DENVIS: scalable and high-throughput virtual screening using graph neural networks with atomic and surface protein pocket features

Agamemnon Krasoulis,[*,†,‡] Nick Antonopoulos,[†,‡] Vassilis Pitsikalis,[†] and Stavros Theodorakis[†]

†*DeepLab, Leoforos Syngrou 106, Athens, Greece*

‡*Contributed equally to this work*

E-mail: a.krasoulis@deeplab.ai

Abstract

Computational methods for virtual screening can dramatically accelerate early-stage drug discovery by identifying potential hits for a specified target. Docking algorithms traditionally use physics-based simulations to address this challenge by estimating the binding orientation of a query protein-ligand pair and a corresponding binding affinity score. Over the recent years, classical and modern machine learning architectures have shown potential for outperforming traditional docking algorithms. Nevertheless, most learning-based algorithms still rely on the availability of the protein-ligand complex binding pose, typically estimated via docking simulations, which leads to a severe slowdown of the overall virtual screening process. A family of algorithms processing target information at the amino acid sequence level avoid this requirement, however at the cost of processing protein data at a higher representation level. We introduce deep neural virtual screening (DENVIS), an end-to-end pipeline for virtual screening using graph neural networks (GNNs). By performing experiments on a benchmark database,

we show that our method performs at least competitively or outperforms several docking-based, machine learning-based, and hybrid docking/machine learning-based algorithms. By avoiding the intermediate docking step, DENVIS exhibits several orders of magnitude faster screening times (i.e., higher throughput) than both docking-based and hybrid models. When compared to an amino acid sequence-based machine learning model with comparable screening times, DENVIS achieves dramatically better performance. Some key elements of our approach include protein pocket modelling using a combination of atomic and surface features, the use of model ensembles, and data augmentation via artificial negative sampling during model training. In summary, DENVIS achieves state-of-the-art virtual screening performance, while offering the potential to scale to billions of molecules using minimal computational resources.

Introduction

In the pharmaceutical industry, the average cost associated with the development of a new drug is approximately $2.6 billion. At the same time, success rates at the final clinical trial stage are typically below 10%[1]. One of the early phases of drug discovery concerns high-throughput screening, a process by which a large number of chemical or biological substances are tested against a specified target of interest. Machine learning has the potential to substantially accelerate the drug discovery life cycle by performing virtual screening of large databases of candidate molecules against a pharmacological agent (e.g., a protein) associated with some known disease[2]. Virtual screening refers to the process by which existing compounds, potentially with some known properties, are utilised to treat novel diseases[3,4]. The special case where the studied compounds have undergone clinical testing and acquired approval from regulatory bodies (e.g., FDA) is referred to as drug repurposing. The outbreak of the COVID-19 pandemic has revealed an utmost need for developing quick and efficient response strategies against emerging diseases using the virtual screening paradigm. Since the outbreak, an unprecedented global effort has been put into using computational methods

to screen vast compound libraries in order to identify candidate molecules for COVID-19 treatment[5].

Virtual screening can be divided into structure-based and ligand-based. Structure-based virtual screening (SBVS) seeks to capture protein-ligand interactions by using, for example, x-ray crystallography measurements to build models that can generalise to novel target-compound pairs[4,6]. On the other hand, ligand-based virtual screening (LBVS) exploits statistical relationships between ligands that are known to bind to a specific target with the aim of predicting binding properties of novel ligands for the same target[7].

Traditional approaches for SBVS employ empirical scoring functions and molecular docking simulations to predict binding affinity scores for a target-ligand pair under various docking conformations[8]. Several docking algorithms are currently commercially available[9–12]. Over the last decade, the use of machine learning has been proposed as a means of building upon this approach to achieve higher predictive performance. To that end, a wide variety of machine learning algorithms have been used, ranging from random forests[13], feed-forward multi-layer perceptrons (MLPs)[14], convolutional neural networks (CNNs)[15–21], and graph neural networks (GNNs)[22–25]. Methods based on deep learning are becoming increasingly popular in this domain. For instance, GNINA[16,20,21] and KDEEP[17] use three-dimensional (3D) CNNs for binding affinity prediction. The input to both models is a 3D voxel representation of a protein-ligand interaction structure, which is typically estimated by a docking algorithm. In a similar fashion, OnionNet extracts atomic features from 3D representations of protein-ligand complexes, which are then processed by a series of convolutional and fully connected layers to predict binding affinity scores[19]. In addition, methods based on GNNs have been increasingly used in virtual screening applications. The atomic CNN makes use of the 3D protein-ligand complex structure and a specially designed graph convolutional network to predict the binding affinity of the complex[15]. Similarly, Torng and Altman[23] employ an amino acid GNN to represent protein pockets and use it in a binding classification task. Finally, Morrone et al.[25] use a dual-graph approach to combine protein-ligand docking pose and ligand structure with

dedicated GNNs, which are then used in a binding binary classification task.

A limitation of this family of methods is that they typically require either access to the experimental crystal structure[15,17,22,24] or rely on docking simulations to estimate the protein-ligand binding pose[16,18–20,25]. Docking simulations are typically very slow and therefore greatly decrease the throughput of the overall screening pipeline. For instance, McNutt et al.[21] report an average computational time of approximately 25 - 29 s for predicting the binding affinity score of a single protein-ligand pair with GNINA. Unfortunately, the high computational cost associated with docking-based methods can hinder the scalability of the virtual screening pipeline, unless huge computational resources (i.e., several thousands of GPUs) are available[26].

A separate line of research has investigated the prediction of protein-ligand binding properties by processing target amino acid sequences and ligand two-dimensional structures, for example, using the SMILES representation. This approach ignores the protein and ligand 3D structure altogether. For example, DeepDTA represents protein sequences and ligand SMILES using sets of words that are then processed by CNNs[27]. WideDTA extends this model by including additional textual features in the protein and ligand representations[28]. PADME combines compound and protein sequence composition features into a combined vector and uses a feed-forward MLP to predict binding affinity scores. A variant of the model uses two-dimensional structural information for ligands, but not for proteins[29]. In addition, DeepConv-DTI uses a convolutional layer to process protein sequences and a fully connected layer for drug fingerprint descriptors that are then combined using a fully connected layer to estimate binding affinity scores[30]. DeepAffinity achieves the same objective by using a structural property sequence representation and a combination of convolutional and recurrent layers.[31] More recently, GNNs algorithms operating on protein sequence data have also been used, including models such as GraphDTA[32], DGraphDTA[33] and MONN[34]. While sequence-level models avoid the requirement for docking simulations, this comes at the cost of processing protein information at a higher representation level (amino acid sequence as

opposed to atom domain). Despite that promising results have been reported using this family of models, a performance comparison between atom-level and sequence-level algorithms is currently missing from the literature.

In this work, we introduce deep neural virtual screening (DENVIS), a purely machine learning-based, high-throughput, end-to-end-strategy for SBVS using GNNs for binding affinity prediction. Our method does not require access to the experimental protein-ligand crystal structure, neither uses docking simulations to estimate it; hence, it is readily-applicable to real-life situations and also highly-scalable. The main contribution of our work can be summarised as follows:

- development of an end-to-end virtual screening system with highly-competitive performance and extremely fast screening times;
- fusion of multiple protein pocket representations (atomic and 3D surface) in combination with ensemble modelling;
- a data augmentation scheme employing artificial negative sampling during binding affinity network training;
- a systematic benchmark of a wide range of docking-based, machine learning-based, and hybrid docking/machine learning-based algorithms for virtual screening, by employing a cross-database validation strategy[35] and using an appropriate baseline model[36,37].

We show that DENVIS achieves at least competitive, and in many cases better performance than several methods, including both research and commercial docking algorithms, but exhibits three to four orders of magnitude faster screening times. We additionally show that our method largely outperforms a purely machine learning-based approach with comparable screening times. We showcase the key components of our method by performing extensive ablation studies, and finally discuss implications and directions for future work.

Methods

DENVIS high-level overview

We tackle the virtual screening problem via ranking of all possible ligands for each target protein. The ranking is performed using estimates of binding affinity scores for all protein pocket-ligand pairs for a given target. We utilise GNNs to extract high-dimensional, continuous vector representations for ligands and protein pockets separately. These vectors are then combined via an outer product layer and passed onto a regression network predicting multiple binding affinity metrics for each protein pocket-ligand pair (Figure 1(a)).

We follow two modelling approaches for protein pockets, one based on atomic features and another one based on 3D surface representation. We term these two models *atom-level* and *surface-level*, respectively. The atom-level model consists of a modified version of the graph isomorphism network (GIN)[38], a generic, yet powerful GNN implementation that has been used in biological and chemical applications[39]. We adopt the feature extraction pipeline of the open graph benchmark[40] for molecules. The surface-level approach utilises a mixture model network (MoNet)[41], a specialised GNN with a convolution operation that respects the geometry of the input manifold. We extract chemical and geometrical features from the protein pocket surface mesh[42]. For ligand feature extraction, we follow the atom-level approach (Figure 1(b)).

Our complete pipeline combines predictions of the two protein pocket representation approaches with late fusion. We first train models with the two approaches independently. The final score for a protein pocket-ligand pair is then computed as a weighted average score of the two different models. We additionally use model ensembles, whereby several identical networks are trained independently with different random seeds for each of the atom- and surface-level models (Figure 1(c)).

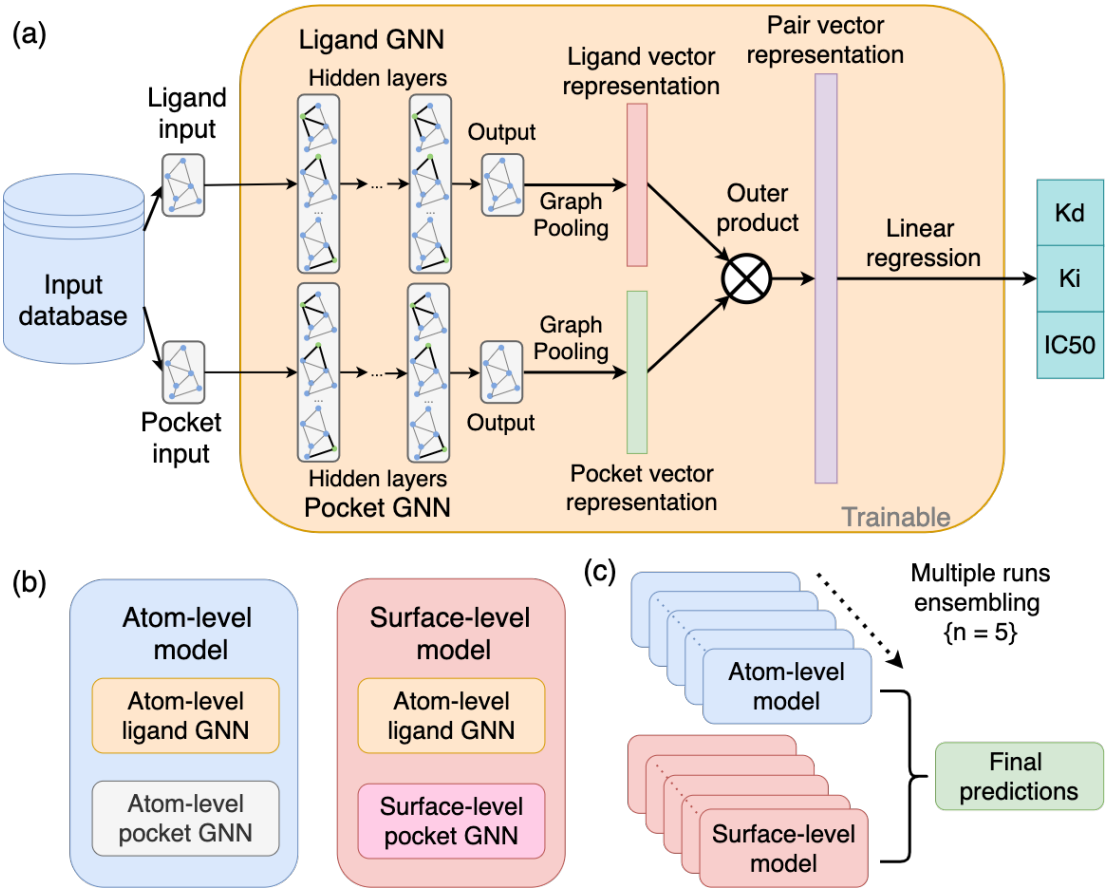

Figure 1: **(a)** DENVIS schematic representation. Ligand and protein pocket features are initially fed to dedicated GNNs. Each GNN yields a graph output which is converted to a vector representation via graph average pooling. The two vectors are then combined via an outer product operation to get a representation for the protein pocket-ligand pair. This final representation is fed to a multi-output linear regression layer to estimate multiple binding affinity metrics. These are K_d, K_i and IC_{50} when the network is trained on the PDBbind general set, and K_d and K_i when it is trained on the PDBbind refined set. **(b)** Two types of representations and associated GNN models are used for protein pocket data processing: atom-level and surface-level. For ligands, the atom-level approach is used. **(c)** Schematic representation of our combined ensembling strategy for virtrual screening. We train five model instances with different random seeds for both atom- and surface-level approaches. To estimate the final binding affinity prediction score for each type of network, we compute the average scores across the five instances. The final binding affinity prediction scores are computed using a weighted average of the atom- and surface-level ensemble model scores.

Datasets

We utilise several different datasets in various steps of our overall pipeline. Namely, we use TOUGH-M1[44] for protein pocket and ligand GNN pre-training, the PDBbind v2019 refined

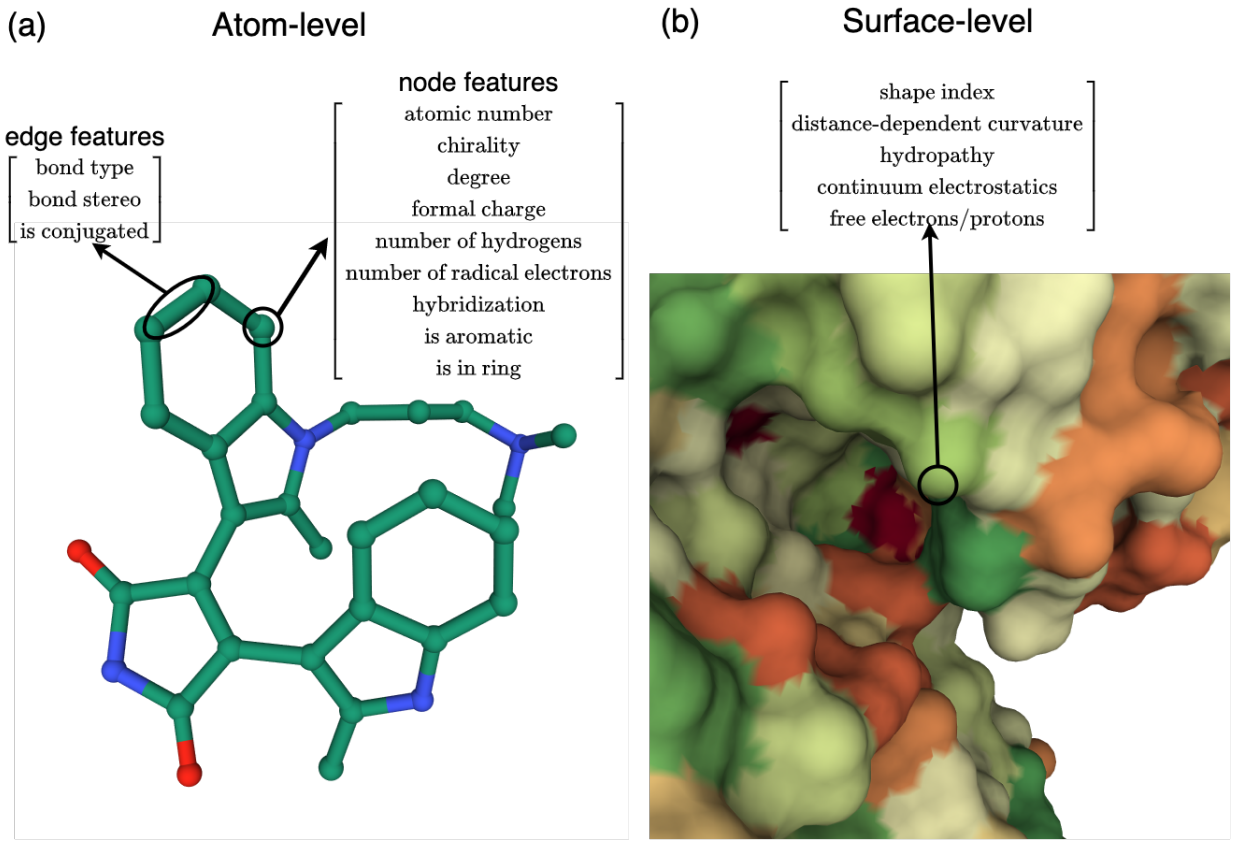

Figure 2: Feature extraction from multiple representations. (a) Atom-level approach. Nine node and three edge categorical features are extracted from the raw structural data, for both protein pockets and ligands[40]. (b) Surface-level approach. Two geometrical and three chemical features are extracted from the protein pocket surface[42]. Visualisations are created using the Mol* tool[43], available on the PDB website, and correspond to the human protein kinase C beta II complexed with a bisindolylmaleimide inhibitor (PDB code: 2i0e).

Table 1: Pre-training and training datasets

Dataset	# Complexes	# K_d	# K_i	# IC_{50}	Used for	Ref.
TOUGH-M1	7524	n/a	n/a	n/a	pre-training	[44]
PDBbind general set	17679	6455	4669	6555	training	[45]
PDBbind refined set	4852	2464	2388	0	training	[45]

and general sets[45] for binding affinity network training (i.e., training sets), the PDBbind v2019 core set[47] for model selection (i.e., validation set), and finally DUD-E[46] for model evaluation and benchmarking (i.e., test set). The characteristics of the various datasets used in this work are summarised in Tables 1 and 2.

Table 2: Validation and test datasets

Dataset	# Targets	# Actives/target	# Decoys/active	Used for	Ref.
PDBbind core set	57	5	56*	validation	[45]
DUD-E	102	224 (average)	50	testing	[46]

* Decoys shared across targets.

Pre-training dataset: TOUGH-M1

TOUGH-M1 is a database designed for binding site matching[44]. It consists of 7,524 distinct pocket structures for which binding ligands are known. These are grouped according to the similarity of their binding ligand resulting in 505,116 pocket pairs with similar binding ligands (positive) and 556,810 pocket pairs with dissimilar ligands (negative). We use this dataset for pre-training protein pocket and ligand GNNs.

Training and validation datasets: PDBbind

PDBbind is a database with selected entries in the protein data bank (PDB) with protein-ligand complex structures. It comprises complexes for which binding affinity has been experimentally verified using one of three measures: dissociation constant (K_d), inhibitor constant (K_i), and half maximal inhibitory concentration (IC_{50})[48]. The database is updated on a regular basis to include recent additions to PDB and is split into three subsets, namely, general, refined, and core sets, with increasingly stricter criteria in data quality for inclusion. Among them, only the general set includes complexes with IC_{50} affinity measurements. In this work, we use v. 2019 of the database[45], which comprises 17,679, 4,852, and 285 complexes in the general, refined, and core sets, respectively. We experiment with both the refined and general sets for model training and use the core set as a validation set for model selection. When using the general set, we only consider protein-ligand complexes and completely discard other types of structures (e.g., protein-protein complexes).

Test dataset: DUD-E

The Directory of Useful Decoys: Enhanced (DUD-E)[46] is a widely-used virtual screening database. It consists of 102 protein targets with an average of 224 active ligands per target. For each active ligand, there are 50 decoys (i.e., inactive compounds) with similar physical properties, but different chemical structures, which are considered to be non-binders. This results in over a million protein-ligand pairs that can be used for screening evaluations. No binding affinity measurements are provided with this dataset. We use DUD-E as a benchmark test set for evaluating and comparing performance against other methods[13,14,21].

Preprocessing and feature extraction

The various datasets that we use have been processed using slightly different pipelines. To avoid systematic discrepancies arising from differences in preprocessing steps and ensure homogeneity across datasets, we perform a common preprocessing pipeline for all protein structures. Firstly, we download the raw protein data from a common source, namely the PDB. For the specific datasets that we use, protein structures in the PDB are typically available as part of a protein-ligand complex. We then protonate the protein data[48] and remove any atom that is not part of the protein.

Similarly, we follow a consistent methodology for pocket extraction to avoid differences across datasets. It should be noted that our modelling approach is agnostic to the used pocket extraction method. Since in our case we have access to protein-ligand complexes, we follow the the PDBbind database creation procedure and keep the atoms of the protein that are a maximum of 10 Angstrom distance from the bound ligand[45]. In cases where no complex structure is available, the pocket could be extracted using any binding site detection algorithm, such as Fpocket[49].

As explained earlier, and also illustrated in Figure 2, we process protein pocket information using two distinct levels of representation: atom-level and protein surface-level. For ligand feature extraction, we employ the atom-level approach. The following sections describe the

two feature extraction pipelines.

Atom-level feature extraction

In the atom domain, we extract nine node and three edge features for each molecule (protein pocket or ligand)[40]. The node features include the atomic number, chirality tag, degree, formal charge, number of explicit hydrogens, number of radical electrons, hybridisation, and two binary features indicating whether the atom is aromatic and whether it is in the ring. The edge features include the bond type, bond stereochemistry, and a binary feature indicating whether the bond is conjugated (Figure 2(a)). All atomic node and edge features as treated as categorical variables.

Surface-level feature extraction

With our surface-level approach, we extract both geometrical and chemical features for the protein pocket surface[42]. Geometrical features consist of the shape index and the distance-dependent curvature, which is an 8D vector. Chemical features include hydropathy, continuuum electrostatics, and free electrons/protons (Figure 2(b)). We then only keep the binding interface defined as the surface nodes that are a maximum distance of 3 Angstrom from the bound ligand. Note that in this case, graph nodes correspond to vertices on the extracted 3D surface mesh, as opposed to the atom-level case, where the nodes correspond to atoms in the molecular structure.

In some complexes, ligands are bound in the interior of the protein and, as such, do not interact with the protein surface. Surface level preprocessing is impossible in this case, and thus we omit those proteins from our surface-level models. This results in eight out of 102 targets from the DUD-E dataset being discarded. For these targets we base our predictions entirely on the atom-level models. For surface-level model training, we discard 691/17679 and 256/4852 complexes from the PDBbind general and refined sets, respectively, due to issues related with pocket surface extraction.

Graph neural network architectures

We use two types of GNNs processing information at the two levels of representation: atom-level and protein surface-level. The atom-level GNN is used for both protein and ligand inputs, whereas the surface-level GNN is only used for proteins.

Atom-level model

For the atom-level GNN, we use our own modified version of the GIN layer[38], which additionally supports edge feature updates at each layer. Briefly, at each GIN layer the features of every node are summed with the corresponding features of the neighbouring nodes and fed into a shallow feed-forward network (i.e., two-layer MLP with ReLU activation), which computes the updated node features. In parallel, the features of each node and the summed features of its neighbours are concatenated with the edge features and fed into a separate, yet identical, MLP to compute the updated edge features.

All atom and edge features are categorical variables[40]. Thus, the first component of the atom-level GNN comprises a collection of embedding layers that convert the categorical variables into continuous vectors. The output size of each embedding layer is computed using the following empirical rule[50]:

$$emb_{dim} = min\{600, round\left(1.6 * n_{cat}^{0.56}\right)\}, \tag{1}$$

where emb_{dim} denotes the embedding layer output dimensionality, and n_{cat} is the cardinality of the categorical variable. The outputs of all embedding layers are concatenated along the feature dimension. Using the empirical rule in Equation 1, the dimension of the continuous node and edge feature vectors are $d_{node} = 56$ and $d_{edge} = 10$, respectively. The node and edge feature vectors are then fed to a series of five blocks comprising a GIN layer, a batch normalisation layer, a ReLU activation function, and a dropout layer. After the final block, where the activation function is omitted, a graph vector representation is computed using a

graph average pooling operation. The node feature dimensionality is progressively increased at each layer in a linear fashion, such that the final vectors have dimensionality $d_{emb} = 300$.

Surface-level model

For our surface level model, we use the MoNet architecture, which is a specialised network that performs a geodesic convolution on the protein surface with learnable gaussian kernels[41]. Briefly, the filters on a geodesic convolution are calculated with respect to distances between points on the surface manifold, as opposed for example to distances in a Euclidean space. The surface input consists of chemical and geometric features extracted from the patch that is adjacent to the bound ligand. We use a 2 layer MoNet with output dimensionality $d_{emb} = 32$[42]. As with the atom-level GNN, the final protein vector representation is obtained with a graph average pooling operation.

Graph neural network pre-training

We use the TOUGH-M1 dataset to pre-train three separate GNNs: 1) atom-level protein pocket GNN; 2) surface-level protein pocket GNN; and 3) atom-level ligand GNN. The three pre-trained networks are then used to initialise the weights of the respective components of the binding affinity networks described below. The pre-training procedure is performed independently for each of the three GNNs. Our motivation for employing network pre-training stems from the fact that the number of labelled samples in the training set (i.e., PDBbind) is rather limited (in the order of a few thousand). Therefore, our goal is to obtain a good model parameter initialisation for binding affinity network training (i.e., fine-tuning).

Since the TOUGH-M1 dataset is organised in similar/dissimilar pairs of protein pockets and, additionally, similar/dissimilar pairs of ligands, we follow a supervised metric learning approach based on Siamese networks[51]. It should be emphasised that this training procedure is fundamentally different to the one used for binding affinity network training, in which case input data come in protein pocket-ligand pairs and the labels are the corresponding binding

affinity measurements. In contrast, during network pre-training, input data come in protein pocket pairs, in the case of protein pocket GNNs, or ligand pairs, in the case of the ligand GNN. The target labels are in this case binary, indicating whether two molecules (protein pockets or ligands, depending on which GNN is being pre-trained) are similar or dissimilar. During pre-training, the two feature vectors corresponding to the two molecules in the pair are fed to the same GNN to compute the corresponding embedding vectors, which are then used to compute the Euclidean distance between the molecules in the embedding space. The objective of the training procedure is to enforce pairs of similar molecules to be closer in embedding space (i.e., have smaller distance) than pairs of dissimilar ones. To that end, we employ the normalised temperature-scaled cross-entropy (NTXEnt) loss function[52].

We adopt a transitive similarity approach to identify similar/dissimilar pairs within a batch. That is, we label as similar/dissimilar all possible pairs that can be inferred from the batch, as opposed to using only the ones that are explicitly defined. Consider, for example, a batch with two pairs (A, B) and (B, C), with corresponding labels "similar" and "dissimilar". By using the transitive similarity approach, the pair (A, C) will be also labelled as "dissimilar" and will be used in the computation of the loss function. For model pre-training we use an Adam optimiser with learning rate of 0.001, a batch size of 8, and train for 10 epochs. We set the value of the temperature hyper-parameter of NTXEnt loss to 0.07.

Binding affinity prediction networks

A high-level overview of our system is shown in Figure 1(a). In this section we provide the details of our implementation and the training procedure.

We use the PDBbind dataset to train our binding affinity prediction networks and experiment with both the refined and general sets for training. All binding affinity measurements are converted to negative log-scale using a base of 10, that is, we perform the transformation $pK = -\log_{10}\{K_d, K_i, IC_{50}\}$. We use all protein pocket-ligand pairs from the training datasets (general or refined) and refer to them as *positive* examples. Moreover, we generate artificial

negative examples during training by combining protein pockets and ligands from different complexes and assigning them a negative log-binding affinity score of 0. That is, we make the following assumptions: 1) protein pockets and ligands from different complexes do not bind; and 2) for non-binding protein pocket-ligand pairs the corresponding binding affinity score is $-\infty$. A different set of negative examples is sampled at the start of every training epoch, while the ratio of positive/negative examples is kept equal to 1 throughout training.

As noted in the previous sections, we use two distinct representations for target protein pockets. Hence, we train two networks independently, one using atomic features and a separate one using 3D surface features. We term these two networks *atom-level* and *surface-level* models, respectively. Each model comprises two sub-networks encoding protein pocket and ligand features into continuous vectors, which are initialised using the pre-training procedure described in the previous section. The protein pocket and ligand vector representations are then combined using an outer product operation. The resulting pair vector represntation is fed to a dropout layer and finally to a fully connected linear layer with multiple outputs, each one corresponding to one binding affinity measure. These are K_d, K_i, and IC_{50} when the networks are trained on the PDBbind general set, and K_d, K_i when they are trained on the PDBbind refined set (Table 1). Our design choice for a multi-output network is based on: 1) biological intuition regarding the different nature of the three binding affinity metrics, especially between IC_{50} and the other two metrics[53]; and 2) the qualitative observation that these follow different distributions (Supplementary Figure S1). We observe that the three binding affinity metrics have similar ranges and, thus, assign an equal weight to the loss term associated with each network output. The overall loss is then computed as:

$$\mathcal{L}_{total} = MSE_{K_d} + MSE_{K_i} + MSE_{IC_{50}},$$

where MSE denotes mean squared error, and the $MSE_{IC_{50}}$ term is omitted in the case of the PDBbind refined set.

For our ensembling modelling approach (Figure 1(b)), we train multiple model instances using different random seeds for negative sample augmentation (and weight initialisation in one of our ablation studies). Based on preliminary analysis using the PDBbind core set as a validation set, we find that performance plateaus at around the point $M = 5$, where M denotes the number of model instances in the ensemble (Supplementary Figure S2). Thus, we choose to use five models for each of the atom- and surface-level ensembles, as this offers a good trade-off between performance and inference time, which scales linearly with M.

Unless noted otherwise, we train our networks for 600 epochs using the Adam optimiser with learning rate of 0.001 and a batch size of 8. We set the weight decay to 0.001 and dropout probability to 0.3 throughout the networks.

Virtual screening strategy

Once our binding affinity networks have been trained, we use them to perform virtual screening. As described in the previous section, our networks have either two or three outputs corresponding to the binding affinity measures available in the training dataset(s). For a specified network and protein-ligand pair, the final predicted affinity score is computed as the unweighted average of the outputs of the network. For each of the two network types (atom-level and surface-level), we run inference on the query protein-ligand pair separately for each of the five model instances and compute the unweighted average scores across the different models (i.e., *multiple runs ensembles*). Finally, we compute a weighted average score of the atom-level and surface-level models. In mathematical terms, the predicted negative log binding affinity score $\hat{y}$ (unitless) for a protein pocket-ligand pair (p, l) is estimated as follows:

$$\hat{y}(p,l) = \alpha_{atom} \sum_{m=1}^{M} \sum_{k=1}^{K} f_{atom}^{m}(p,l)\,[k] + (1-\alpha_{atom}) \sum_{m=1}^{M} \sum_{k=1}^{K} f_{surface}^{m}(p,l)\,[k]\,, \tag{2}$$

where f^m_{atom} and $f^m_{surface}$ denote the mth instance of the atom-level and surface-level models, respectively, k indexes the outputs of each of the models, $K = 3$ is the number of model outputs (or $K = 2$ for models trained on the PDBbind refined set), $M = 5$ is the number of model instances trained for each configuration, and α_{atom} is the weight coefficient for the atom-level model, which is set *a priori* to $\alpha_{atom} = 0.5$. For targets for which surface preprocessing is not successful, we set $\alpha_{atom} = 1.0$ (eight out of 102 DUD-E targets).

Once binding affinity scores have been estimated using Equation 2, ligands are ranked in decreasing binding affinity prediction order on a per-target basis. The resulting per-target ligand rankings are then used to compute the three performance scores introduced in a later section.

Efficient virtual screening implementation

We implement an efficient screening strategy for our method. That is, we first compute the vector representations for each protein pocket and ligand in the screening dataset and store them in memory. Then, for each protein pocket-ligand pair query, we retrieve the corresponding vectors from memory and feed them to the interaction outer product layer and final linear layer. This enables us to reduce inference times, since most computation is spent on extracting the vector representations from the protein pocket and ligand graph data. This efficient strategy can be adapted, if required, such that only target protein vector representations are pre-computed and stored in memory. This is useful in cases where the screening dataset has a small number of targets, but a very large number of ligands that cannot fit in memory (e.g. DUD-E). Even in this case, pre-computing protein pocket vectors can be very efficient as compared to the naive case where protein pocket vectors are computed afresh, due to the comparatively larger size of protein pocket graphs, which leads to a higher computational cost for the protein pocket GNN.

Evaluation

Performance metrics

We use three metrics for performance evaluation: area under receiver operating characteristic curve (AUROC), enrichment factor (EF) and Boltzmann enhanced discrimination of ROC (BEDROC). All three metrics are computed separately for each target protein and, unless noted otherwise, median scores across targets are reported (i.e., *micro-averaging*). To compute AUROC and BEDROC scores for a given target we use the sorted list of predicted binding affinity scores. It should be noted that although these scores do not correspond to binding probabilities, they can still be used for the computation of the two metrics.

The use of AUROC has been often criticised in virtual screening applications, as this metric assigns equal weight to all ligands in the screening library without taking into account their ranking. Thus, the metric does not take into consideration the fact that only a small fraction of top-ranked ligands will be experimentally validated (i.e., *early recognition*). To address this issue, BEDROC uses exponential weighting to assign larger weights to early rankings[54] as follows:

$$BEDROC_\alpha = \frac{\sum_{i=1}^{NTB_t} e^{-\alpha r_i/N}}{R_\alpha \left(\frac{1-e^{-\alpha}}{e^{\alpha/N}-1}\right)} \times \frac{R_\alpha \sinh(\alpha/2)}{\cosh(\alpha/2) - \cosh(\alpha/2 - \alpha R_\alpha)} + \frac{1}{1-e^{\alpha(1-R_\alpha)}}, \qquad (3)$$

where NTB_t is the total number of true binders (actives), N is the total number of ligands, $R_\alpha = NTB_t/N$ is the ratio of actives in the screening library, and r_i is the rank of the ith active moleclue. We set $\alpha = 80.5$, which results in the 2% top-ranked ligands accounting for 80% of the BEDROC score[55].

The EF is another screening power metric which evaluates the ability of a screening algorithm to identify true binders among the top-ranked ligands[56]. That is, it is related to the widely used recall metric, but only considers a subset of top-ranked ligands. The EF

metric is defined as follows:

$$EF_\alpha = \frac{NTB_\alpha}{NTB_t \times \alpha}, \tag{4}$$

where NTB_α is the number of true binders in the top $\alpha\%$ (e.g., $\alpha = 1\%$, 5%, or 10%) and, as above, NTB_t is the total number of true binders in the screening library. We choose $\alpha = 1$ and thus evaluate recall among the top 1% of our ranking list.

Benchmark

We use the DUD-E database as a benchmark to compare the virtual screening performance of DENVIS against several competitive methods, falling into three main categories: 1) docking algorithms (AutoDock Vina[57], Gold,[9] Glide,[11] FlexX,[12] Surflex[10]); 2) hybrid docking/machine learning-based algorithms (GNINA[21], RF-score[13], NN-score[14]); and 3) a purely machine learning-based algorithm (DeepDTA[27]). Note that GNINA, RF-score, and NN-score require the binding pose of the query protein-ligand pair and for this purpose they make use of AutoDock Vina binding pose predictions. GNINA uses a 3D CNN applied to the docked protein-ligand pose, whereas RF-score and NN-score improve upon AutoDock Vina binding affinity estimates by using a random forest and a shallow feed-forward network, respectively.

For the four commercial docking methods (i.e., Gold, Glide, FlexX, and Surflex), we use the predictions from Chaput et al.[55]. For AutoDock Vina, RF-score, and NN-score, we use the results from Ragoza et al.[16]. Finally, for GNINA, we use the results reported by McNutt et al.[21].

To compute binding affinity predictions for the DUD-E database with DeepDTA, we make use of the DeepPurpose library[58]. In contrast with all other methods in the benchmark, which make use of structural protein and ligand information, DeepDTA is a sequence-level model and makes predictions by processing the target amino acid sequence and SMILES strings. We experiment both with the model provided by DeepPurpose which, as originally proposed by the authors is pre-trained on the DAVIS dataset[59], as well as our own version of the model that we train from scratch on the PDBbind refined set. We use a learning rate of

10^{-4}, a batch size of 256, and train the network for 600 epochs.

Ligand baseline

We additionally assess the performance of a simple ligand baseline model. To that end, we train binding affinity networks by removing the protein pocket GNN altogeher. That is, the model learns to assign binding affinity scores to ligands without considering any type of protein information. Such ligand-based baselines have been previously proposed as a means of quantifying potential dataset biases[36,60]. To avoid considering the same inputs as both positive and negative examples, we switch off negative sampling in this case during training.

Statistical analysis

The DUD-E database comprises 102 targets, which makes it possible to run statistical comparisons for our benchmark with acceptable statistical power. Without making any assumptions about the underlying distribution of AUROC, EF_1, and $BEDROC_{80.5}$ scores, we use the Friedman test to assess the effect of decoding algorithm on performance. We perform post-hoc pair-wise comparisons using the Wilcoxon signed-rank test and the Šidák correction method to account for multiple comparisons.

Results

Virtual screening performance benchmark

We train five instances of atom- and surface-level models using the PDBbind refined and general sets (v. 2019). We run inference using all 10 models on the DUD-E dataset, which comprises 102 targets, and combine their predictions to obtain final predictions (Figure 1(c) and Equation 2). We refer to our ensemble models trained on PDBbind general and refined sets as "DENVIS-G" and "DENVIS-R", respectively. We compare the performance of our ensemble models to all other models in the benchmark and present the overall results in Figure

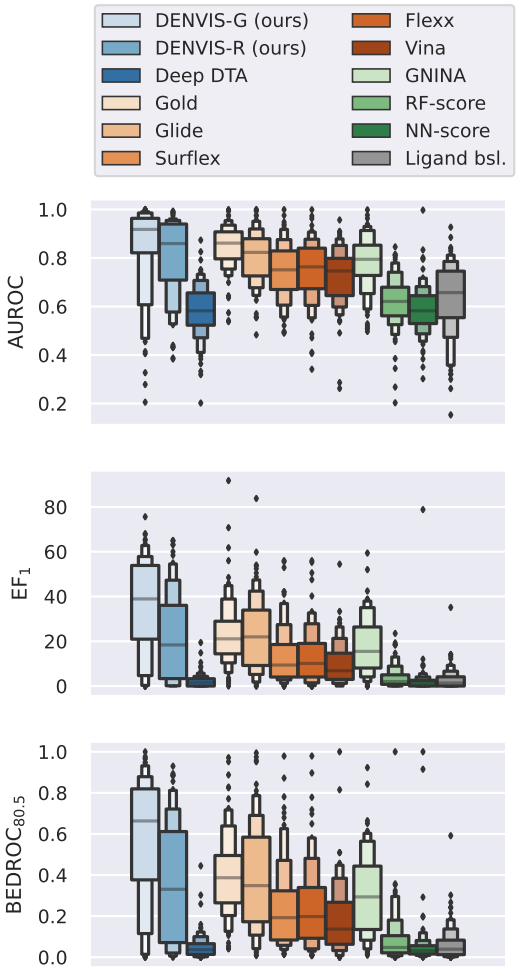

Figure 3: DUD-E virtual screening benchmark. The performance of several methods is shown using the AUROC, EF_1, and $BEDROC_{80.5}$ metrics. Box plots show the score distributions for the 102 DUD-E targets. Grey horizontal lines correspond to medians. Diamonds indicate outliers. Colour code: blues, machine learning-based; oranges, docking-based; greens, hybrid docking/machine learning-based; grey, ligand baseline.

3. Median scores achieved with all methods are also summarised in Table 3. The Friedman test reveals a significant effect of decoding algorithm on performance (AUROC, $p < 10^{-108}$; EF_1, $p < 10^{-120}$; $BEDROC_1$, $p < 10^{-120}$). We perform post-hoc pair-wise comparisons for these three metrics on a subset of model pairs of interest and present the results in Table 4.

DENVIS-G achieves the highest median AUROC performance followed by DENVIS-R, Gold, Glide, and GNINA. It also achieves the highest median EF_1 and $BEDROC_{80.5}$ scores. DENVIS-G significantly outperforms DENVIS-R in all three metrics. DENVIS-R achieves

Table 3: DUD-E virtual screening benchmark summary (median scores)

	AUROC	EF_1	$BEDROC_{80.5}$
DENVIS-G$^{\star, \dagger, \vee}$	**0.92**	**38.92**	**0.66**
DENVIS-R$^{\star, \dagger, \vee}$	0.86	18.37	0.33
Deep DTA$^{\circ, \vee}$	0.58	1.62	0.04
Gold$^{\star, \diamond}$	0.86	21.08	0.39
Glide$^{\star, \diamond}$	0.82	21.96	0.35
Surflex$^{\star, \diamond}$	0.75	9.36	0.19
Flexx$^{\star, \diamond}$	0.76	10.10	0.20
Vina$^{\star, \diamond}$	0.75	6.84	0.14
GNINA$^{\star, \diamond, \vee}$	0.79	15.48	0.29
RF-score$^{\star, \diamond, \vee}$	0.62	2.00	0.05
NN-score$^{\star, \diamond, \vee}$	0.58	1.38	0.03
Ligand baseline$^{\star, \vee}$	0.66	1.31	0.04

G, PDBbind general set; R, PDBbind refined set; *, atom-level protein (pocket) representation; †, surface-level protein (pocket) representation; $^{\circ}$, sequence-level protein representation; $^{\vee}$, machine learning; $^{\diamond}$, docking.

Table 4: Statistical analysis for DUD-E virtual screening benchmark

		AUROC	EF_1	$BEDROC_{80.5}$
DENVIS-G	DENVIS-R	***	***	***
DENVIS-R	GNINA	n.s.	n.s.	n.s.
DENVIS-G	Gold	n.s.	***	***
DENVIS-G	Glide	**	***	***
DENVIS-R	Deep DTA	***	***	***
DENVIS-G	Ligand baseline	***	***	***
DENVIS-R	Ligand baseline	***	***	***
GNINA	Ligand baseline	***	***	***
Deep DTA	Ligand baseline	**	n.s.	n.s.
Vina	Ligand baseline	***	***	***
RF-score	Ligand baseline	n.s.	n.s.	n.s.
NN-score	Ligand baseline	*	n.s.	n.s.
Gold	Ligand baseline	***	***	***
Surflex	Ligand baseline	***	***	***
Flexx	Ligand baseline	***	***	***
Glide	Ligand baseline	***	***	***

*, $p < 0.05$; **, $p < 0.01$; ***, $p < 0.001$; n.s., non-significant. Abbreviations as in Table 3.

slightly higher median scores than GNINA, however the differences are below the significance level. It should be noted that both models have been trained on the same dataset (i.e., PDBbind refined set v. 2019).

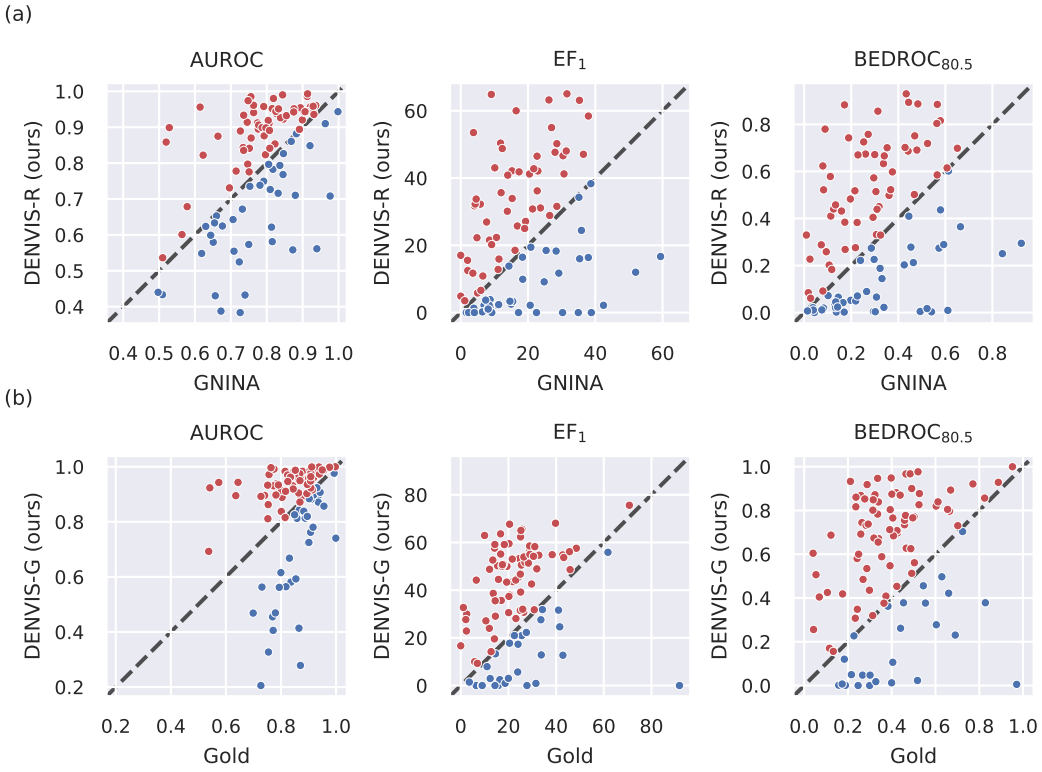

Figure 4: Per-target comparisons using AUROC, EF_1 and $BEDROC_{80.5}$ metrics. (a) Comparison between DENVIS-R and GNINA models. Both models are trained on the PDBbind refined set. (b) Comparison between DENVIS-G and Gold models. DENVIS-G is trained on the PDBbind general set, while Gold is a purely docking-based algorithms and therefore does not require training. Each point in the scatter plots corresponds to a single DUD-E target ($n = 102$), and is coloured to indicate the model that achieves the higher performance (DENVIS, red; GNINA/Gold, blue).

Among the four docking algorithms, Gold and Glide achieve the highest performance. Both models are significantly outperformed by DENVIS-G, except for the AUROC metric which is comparable between DENVIS-G and Gold.

All models achieve a significantly higher AUROC score than our ligand-baseline, with RF-score being the only exception. With respect to EF_1 and $BEDROC_{80.5}$ scores, the following models do not significantly outperform the ligand-based baseline: RF-score, NN-score, and DeepDTA. For the DeepDTA algorithm, we additionally experiment with a model pre-trained on the DAVIS dataset, as was originally proposed by the authors[27]. This model performs worse than the one trained on the PDBbind refined set and considerably worse than our

Table 5: Average virtual screening times per protein pocket-ligand pair

Model	Implementation	Single prediction (ms)	Ensemble prediction (ms)
DENVIS (ours)	efficient	0.314 ± 0.008	1.570 ± 0.039
DENVIS (ours)	naive	1.908 ± 0.003	9.540 ± 0.014
DeepDTA	naive	0.582 ± 0.006	-
Gold[61]	-	1.2×10^3	-
FlexX[62]	-	$\sim 1 \times 10^3$	-
Surflex[63]	-	$\sim$ 1-3 $\times 10^3$	-
Glide[64]	-	$\sim 0.5 \times 10^3$	-
GNINA[21]	-	2.6 - 2.65 $\times 10^4$	2.7×10^4

ligand-based baseline, achieving chance-level median AUROC, EF_1 and $BEDROC_{80.5}$ scores of 0.50, 0.0 and 0.0, respectively (not shown).

Figure 4 shows one-to-one scatter plot comparisons between (a) DENVIS-R and GNINA and (b) DENVIS-G and Gold for the three evaluation metrics of interest. Each point in these graphs corresponds to a single target in DUD-E. Extended per-target performance scores obtained with all algorithms in the benchmark are provided in the Supplementary Material (Supplementary Tables S1, S2, and S3).

Virtual screening times benchmark

We now turn our attention to virtual screening (i.e., inference) times exhibited by a subset of algorithms in our benchmark: DENVIS, DeepDTA, Gold, FlexX, Surflex, Glide, and GNINA. For our method, we employ two strategies for screening, namely, naive and efficient screening. In the naive case, we compute the vector representations for every new protein pocket-ligand pair afresh, whereas with the efficient strategy we pre-compute the vector representations for each target protein pocket and store them to memory (see Methods section). In both cases, once the protein pocket and ligand vector representations have been (pre-)computed, they are fed to the interaction and final prediction layers to obtain the binding affinity prediction scores.

Average screening times for a protein pocket-ligand pair are presented in Table 5. For

Table 6: Ablation studies summary (median scores)

	AUROC	EF_1	$BEDROC_{80.5}$
Multi-ensemble (baseline)	0.86	18.37	0.33
Single model prediction	0.83	12.74	0.26
Without pre-training	0.87	16.67	0.34
Without negative sampling	0.63	1.96	0.05
Binding classification	0.78	9.39	0.20
Level ensemble⋆	0.87	18.48	0.35
Atom-level⋆	0.85	13.33	0.27
Surface-level⋆	0.78	11.07	0.23

⋆ Using subset of target protein pockets for which both atom-level and surface-level features are extracted (94/102 targets).

our method and DeepDTA we measure screening times on a Linux-operated machine (AMD Ryzen Threadripper 2970WX 24-Core Processor, 128 GB RAM, Ubuntu 18.04.4 LTS) using a single GPU (NVIDIA® GeForce® RTX 2080 Ti, 11 GB). We repeat all inference experiments 20 times and report average screening times (mean ± std). For Gold, FlexX, Surflex, Glide, and GNINA, we reproduce the times reported in the original references[21,61–64].

Using the efficient implementation our method achieves an average screening time of 0.314 ms per protein pocket-ligand pair, which includes inference with one atom- and one surface-level model. A single DeepDTA model has nearly double inference times with an average of 0.582 ms. On the other hand, docking algorithms (i.e., Gold, FlexX, Surflex, Glide) exhibit three orders of magnitude higher screening times, that is, between 0.5 and 1.5 s. Inference times with GNINA are four orders of magnitude higher than with our models, in the range of 26-27 s. The inference time of DENVIS scales linearly with the number of model instances in the ensemble, leading to an average of 1.570 ms per protein pocket-ligand pair when using ensembles comprising five atom- and surface-level models (in total 10 models). This exceeds the screening time of a single DeepDTA model by a factor of 3 approximately, while still being several orders of magnitude faster than docking algorithms and GNINA.

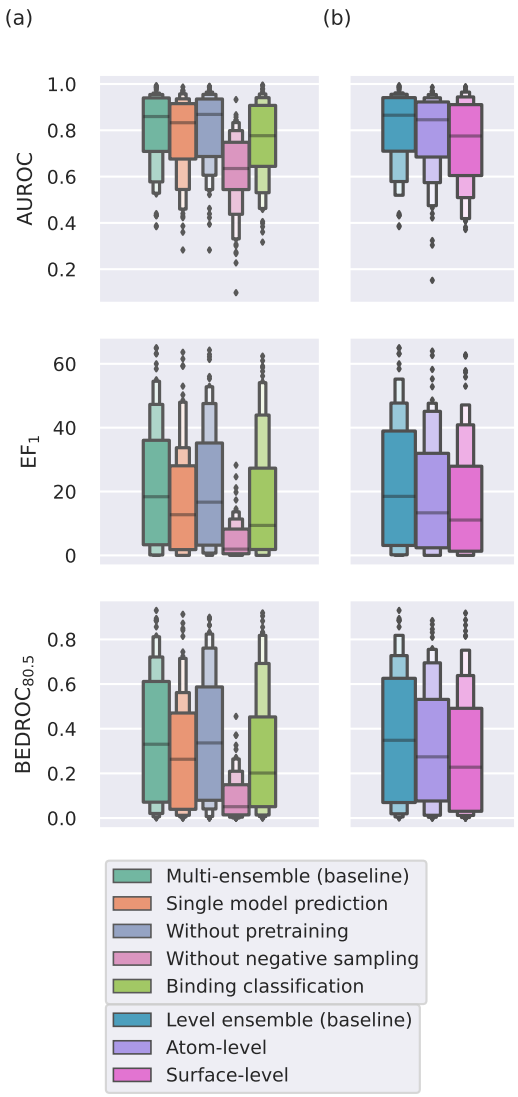

Figure 5: Ablation analysis. (a) Multi-ensemble (baseline) refers to our complete method, the other models either have a component deactivated or some other modification (refer to main text for details). Box plots show score distributions for all DUD-E targets ($n = 102$). (b) Atom-level, surface-level and level ensemble comparison. Only targets for which protein surface preprocessing is successful are included ($n = 94$). All models are trained on PDBbind refined set for 600 epochs.

Ablation studies

We now perform a series of ablation studies to assess the effect of several important design parameters of DENVIS on virtual screening performance. For the purposes of this analysis our baseline is the ensemble atom/surface-level model, for which both models in the ensemble

Table 7: Ablation studies statistical analysis

		AUROC	EF_1	$BEDROC_{80.5}$
Multi-ensemble (baseline)	Single model prediction	***	***	***
	Without pre-training	n.s.	n.s.	n.s.
	Without negative sampling	***	***	***
	Binding classification	***	***	***
Level ensemble	Atom-level	n.s.	***	***
	Surface-level	***	***	***

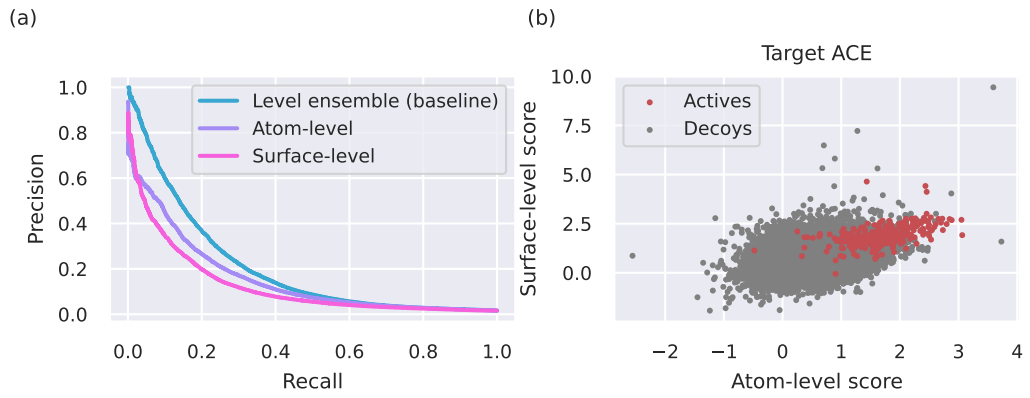

Figure 6: Combination of atom- and surface-level protein pocket representations. (a) The precision-recall curves are shown for the three types of models: atom-level, surface-level, and level ensemble (baseline). Results from aggregated targets are shown ($n = 94$). (b) Scatter plot of predicted scores with atom- and surface-level models for Angiotensin-converting enzyme (ACE) target (PDB code: 3bkl). Each point corresponds to one ligand and the colour code indicates whether the ligand is an active compound or a decoy.

comprise five model instances (i.e., multiple runs ensembling, Figure 1) trained on the PDBbind refined set. The GNN components are pre-trained using the M1 dataset and the metric learning approach described in the Methods section. Finally, during model training, we generate artificial negative examples as described in the Methods section. We refer to this model as *multi-ensemble (baseline)* in Figure 5, and *ME* in Tables 6 and 7.

We experiment with the following modifications to our baseline model: 1) *single model prediction*, whereby the atom- and surface-level models comprise a single model instance (as opposed to five in the baseline model); 2) *without pre-training*, whereby all models are trained from scratch; 3) *without negative sampling*, whereby models are trained using positive

examples only; and 4) *binding classification*, whereby our networks are trained with a binary cross-entropy loss using binary target labels indicating whether a ligand binds to the target protein pocket. Moreover, we compare the performance of *atom-level* (*AL*), *surface-level* (*SL*) and *level ensemble* (*LE*) models. We perform this analysis separately, since in this case we only include in the comparisons the target proteins for which surface-level preprocessing is successful (94/102 DUD-E targets, see Methods section).

The overall results of our ablation studies are presented in Figure 5 and median scores are also summarised in Table 6. The results from the statistical analysis are shown in Table 7. We observe that negative sampling is a key component of our method, since removing it leads to a dramatic decrease in performance. Using single model predictions (one for each of the atom- and surface-level models) also leads to a significant drop in performance. On the other hand, model pre-training does not seem to affect performance significantly (Table 7). Finally, the use of atom/surface-level model ensembles achieves significantly better performance than its atom-level and surface-level counterparts (Table 7).

We now perform further analysis to gain more insight into how combining multiple levels of protein pocket representation enhances the performance of our method. The precision-recall curves for the three types of models, namely, atom-level, surface-level and level ensemble, are shown in Figure 6(a). The curves correspond to aggregated targets for each of the three cases. It can be observed that the level ensemble model has better precision than its single-level counterparts, especially in the region of early ligand rankings (i.e., top-ranked ligands), which corresponds to the left-most area of the graph. Figure 6(b) shows an example of the scores predicted by the atom- and surface-level models for one target (Angiotensin-converting enzyme (ACE), PDB code: 3bkl). Each point in the scatter plot corresponds to one ligand and the colour code indicates whether the ligand is an active compound or a decoy. We observe that true binders tend to receive high scores by both models, which illustrates how the combination of the two models leads to higher precision. A similar behaviour is observed for the majority of target proteins in DUD-E. For the shown target, the atom-level, surface-level

and level ensemble EF_1 scores are 29.43, 11.35, and 32.27, respectively.

Virtual screening evaluation metrics analysis

We observe that our three evaluation metrics, namely AUROC, EF_1, and $BEDROC_{80.5}$ are not always in perfect alignment in their assessments. For instance, DeepDTA and NN-score achieve significantly higher AUROC scores than the ligand-based baseline, however they do not significantly outperform the baseline with respect to the EF_1 and $BEDROC_{80.5}$ metrics (Table 4).

To better understand the potential discrepancies between these three metrics, we study their relation and present the results of this analysis in Figure 7(a),(b). The two scatter plots correspond to the DENVIS-R model and show the linear relationship between (a) AUROC and EF_1 and (b) AUROC and $BEDROC_{80.5}$ scores, for the 102 targets in DUD-E. That is, each point in the scatter plots corresponds to one target protein in the database. In both cases, there is a significant positive correlation between the evaluation metrics, however it is not very strong (i.e., $r < 0.80$ in both cases). Moreover, for both models we observe outliers, which correspond to high EF_1 and $BEDROC_{80.5}$ scores (top-right corners) that lie far from the regression lines. This observation implies that the relationship of the metrics may in fact be non-linear.

We attribute the relative discrepancies between the AUROC and EF_1 metrics to the fact that they consider different (sub-)sets of the data: AUROC is a global metric which considers all available ligands for a given target, whereas EF_1 only considers the top 1% of ranked ligands. On the other hand, the BEDROC is a global metric, that is, it considers all ligands, but uses exponential weighting to assign larger values to early-ranked ligands[54]. To illustrate how these different approaches can influence the measured performance, we provide an example for one target (Protein kinase C beta (KPCB), PDB code: 2i0e) in Figure 7(c) showing the distribution of binding affinity scores predicted by our model. Distributions of the active and decoy sets for this target are shown separately. We observe that, for the

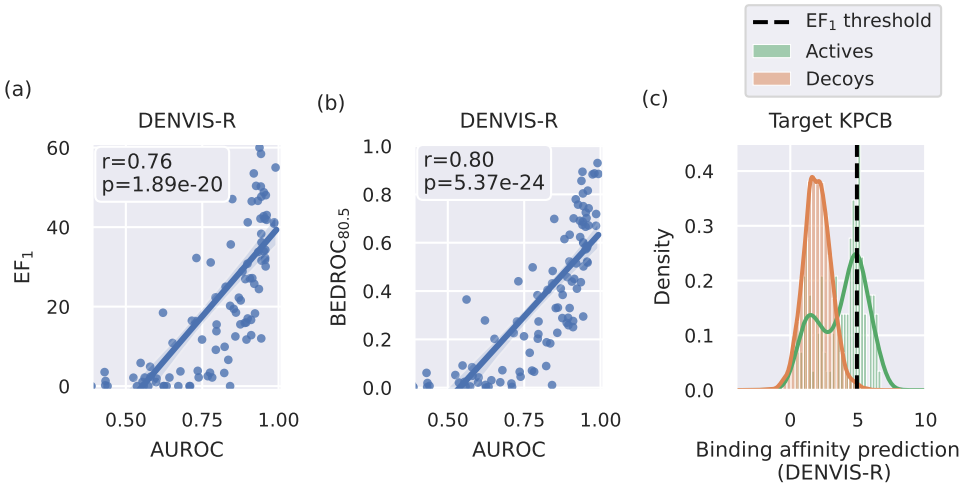

Figure 7: Virtual screening evaluation metric analysis. (a)-(b) Linear relationship between (a) AUROC-EF_1 and (b) AUROC-$BEDROC_{80.5}$ scores using DENVIS-R model predictions. Linear regression fits and 95% confidence intervals are shown using bootstrapping (1000 iterations). Insets indicate the corresponding correlation coefficients (r) and significance values (p). (c) Example distribution of prediction scores using DENVIS-R for Protein kinase C beta (KPCB) target (PDB code: 2i0e). Distribution scores for the active and decoy sets are shown separately. The black vertical line denotes the cutoff threshold used by the EF_1 score (i.e., top 1% of ranked ligands).

shown example, the two distributions overlap highly in the lower score range, however they are clearly separated above the EF_1 cutoff threshold (black horizontal line). This is due to the active set having a heavy tail above this threshold. The resulting AUROC, EF_1 and $BEDROC_{80.5}$ scores for this example are 0.78 and 31.1, and 0.50, respectively.

Discussion

Virtual screening benchmark

In this work, we introduce DENVIS, a GNN-based, end-to-end pipeline for drug virtual screening. In contrast with the majority of SBVS approaches, our method does not rely on docking simulations to estimate target-compound binding poses. By evaluating performance on a benchmark dataset we show that our approach achieves competitive performance to several commercial docking algorithms (i.e., Gold,[9] Glide,[11] Surflex,[10] and Flexx[12]), when it

is trained on the PDBbind refined set. Additionally, it achieves competitive performance to GNINA, a state-of-the-art research algorithm combining docking and a 3D CNN[21]. When trained on the PDBbind general set, our method outperforms all other methods in the benchmark by a large margin, including our own model trained on the PDBbind refined set (Figure 3 and Table 4). This observation is in agreement with previous reports in the literature showing that the inclusion of more data in the training set leads to virtual screening performance improvement[20].

The very fast inference time of our method renders it suitable for virtual screening of massive ligand libraries with minimal computational resources. By avoiding the intermediate docking step, our method exhibits three orders of magnitude faster screening times than state-of-the-art commercial docking algorithms, and four orders of magnitude faster screening times than GNINA (Table 5). We do not have access to screening times for AutoDock Vina, RF-score, and NN-score and therefore do not include them in the screening time benchmark. However, McNutt et al.[21] report an average docking time of 25 s with AutoDock Vina. Given that RF-score and NN-score build upon AutoDock Vina predictions, it is safe to assume that this figure is a lower bound for these two models. When compared to DeepDTA, a language-based method using whole-protein sequences and ligand string representations, which exhibits comparable inference times to our method, we show that we achieve dramatically better screening performance (Figure 3). Taking everything into consideration, it can be argued that our approach combines the best of two worlds, that is, the screening performance of state-of-the-art docking-based and hybrid docking/machine learning-based methods operating at the atomic level, and the throughput of purely machine learning-based models processing protein information at the sequence level.

To further decrease the inference time of our method, we design an efficient screening strategy, whereby protein pocket and/or ligand vector representations are pre-computed and stored in memory. We show that this can further decrease the screening time by approximately a factor of 6. The ability of using such a type of efficient screening stems directly from

the design of our algorithm, which does not take the protein-ligand complex as an input, but rather the two entities separately. This is not possible with docking-based methods, as in that case the protein-ligand binding pose needs to be simulated separately for each protein-ligand pair. Using an earlier version of our system, we screened 1 billion molecules against three SARS-CoV-2 proteins as part of the "JEDI Billion molecules against Covid-19 Grand Challenge"[5]. The whole virtual screening process took less than 48 hours using a single GPU.

Novel aspects of DENVIS, comparison with related models and potential extensions

A few other methods have been recently proposed to circumvent the requirement for docking simulations. For example, Torng and Altman[23] and Li et al.[34] have introduced GNN architectures that model interactions between protein amino acids and small molecule atoms. One main difference between these two methods and ours is that we model interactions at the atomic level for target proteins, as opposed to amino acid sequence level. Another difference lies in the way that the protein and ligand vector representations are combined to produce the final binding affinity estimates. Torng and Altman[23] use a concatenation layer, whereas Li et al.[34] use a dual-attention mechanism in combination with an outer product layer. Attention-based mechanisms have also been proposed in the context of sequence-level models[31].

It should be emphasised that our method is capable of producing accurate binding affinity estimates by considering interactions at the abstract space of protein pocket and compound vector representations rather than at the atomic level. This is due to the fact the protein-ligand interaction layer follows the global graph pooling operations in the two graphs. As a result, our method is binding pose invariant. Recently, a GNN-based method has been proposed for predicting ligand conformations for protein targets[65]. In the future, it shall be interesting to investigate the feasibility of combining this approach with our method in order

to develop a system that can predict both binding pose and affinity simultaneously.

A crucial and novel aspect of our methodology is the use of artificial negative data augmentation, whereby we generate artificial examples of non-binding protein pocket-ligand pairs during training. Our ablation analysis revealed that this is a key element of our approach with regards to its performance on a virtual screening task (Figure 5 and Table 7). This is somewhat expected, as the inclusion of negative examples forces our model to assign low scores to non-binding protein pocket-ligand pairs. In the opposite case, that is, when our model is only trained with binding protein-ligand complexes, the large majority of pocket-ligand pairs at test time (i.e., screening), which correspond to non-biding protein-ligand pairs, will be seen as out-of-distribution input data. For our negative sampling augmentation approach, we make the assumption that pockets and ligands from different complexes in the training set do not bind. In practice, this assumption may be violated, albeit with very small probability. It is nonetheless clear that the benefit of negative sampling on performance largely outweighs the negative effect of the small label noise that may be introduced in the case of false negatives. Notably, we generate a different set of artificial negative examples in each training epoch, while keeping the positive/negative sample ratio fixed, thereby generating millions of negative samples during training. Although it is possible that other methods might benefit from the use of negative sampling augmentation, deploying this technique with docking-based methods would be likely infeasible, since in that case binding poses for all protein-ligand negative pairs would need to be estimated with docking simulations.

Another important contribution of our work is the representation of protein pocket information at two levels, namely, atomic and surface level. To our knowledge, such combination of protein pocket information at multiple levels of representation has not been previously reported. We show that this leads to a dramatic increase in performance (e.g., median EF_1 improvement of 38.6% and 66.9% as compared to atom- and surface-level models, respectively). We observe that combining the two models leads to higher precision (Figure 6). Interestingly, this finding has been previously reported when combining different docking algorithms, a

technique called consensus docking[66]. It is possible that combining fundamentally different models, such as different docking algorithms in consensus docking or, in our case, GNNs taking as inputs different types of protein pocket features, acts as a form of regularisation; errors made by one model can be counter-balanced by predictions from the other model. In our analysis, we observe that where both models agree, by assigning a high score to a specific ligand, the true probability of binding is usually high (Figure 6(b)). To the best of our knowledge, this is the first study combining multiple protein pocket representations for virtual drug screening. Here, we train separate models for the two types of representations and average their predictions at inference (i.e., late model fusion). An alternative approach could be to include both representations in a single multi-modal network and train it end-to-end.

Furthermore, in agreement with previous work[18,20,21,67], we find that using model ensembles leads to an additional improvement in performance (average EF_1 improvement of 29.0%). Since we initialise our model weights using network pre-training, the main difference between the base models in the ensemble is that they are trained using a different collection of artificially generated negative samples – and some stochasticity induced by data shuffling during training. One caveat of using model ensembles is that inference time increases proportionally with the number of model instances in the ensemble. One possible way to overcome this limitation would be to use model ensembles in conjunction with knowledge distillation, whereby a student model could be trained to predict the output of a teacher ensemble model[68,69].

Finally, we find that protein and ligand GNN pre-training using the TOUGH-M1 dataset and our metric learning-based approach does not yield a performance improvement, as one might have expected (Figure 5, Tables 6 and 7). Hu et al.[39] report an increase in performance using the MUV dataset and a combination of node-level and graph-level supervised pre-training. However, it should be noted that the datasets and validation strategies used in the two cases are different and, therefore, not directly comparable. The TOUGH-M1 dataset comprises more than 1M pairs of similar/dissimilar protein pockets and pairs of

similar/dissimilar ligands. However, the number of unique proteins and ligands in the dataset is substantially lower, that is, in the order of a few thousand (Table 1). It is possible that in order to achieve an improvement in virtual screening task performance with our metric learning-based pre-training approach, a much larger pre-training dataset is required. This would allow the protein pocket and ligand GNNs to have access to much richer information about the underlying protein and ligand structure probability distributions during the pre-training phase. Future research will further investigate alternative, self-supervised GNN pre-training strategies and their potential benefit to downstream virtual screening tasks.

Dealing with biases in biochemical datasets

Machine learning-based methods for SBVS are often criticised for being prone to overfitting and failing to generalise to real-world scenarios[35–37,60,70–73]. Model validation is far from being an easy task, as there exists strong evidence demonstrating that performance reported for machine learning-based algorithms is heavily affected by biases in the used biochemical datasets. A typical example is the comparative assessment of scoring functions (CASF) virtual screening benchmark[45,47,74], which uses the refined and core subsets of the PDBbind database[48] as the training and test sets, respectively. At the time it was first proposed[74], the majority of scoring algorithms used empirical functions. High performance has since been reported with a wide variety of machine learning methods[47], however it has been suggested that this observation may be largely attributed to the similarity between targets in the training and test sets[70,72]. Moreover, it has been found that binding affinity prediction algorithms trained on the PDBbind refined set might perform well on the core set, but fail to generalise to other virtual screening datasets[71]. For that reason, an alternative benchmark is deemed necessary.

Other common forms of bias are analogue and decoy bias. Analogue bias refers to the case where a dataset may contain many analogue active ligands with the same chemotype. A machine learning model trained to recognise one such ligand as active for a given target is

likely to assign high binding probability and/or affinity scores to the remaining ligands in the same scaffold[75]. On the other hand, decoy bias, or artificial enrichment, refers to the case where active and decoy sets are different in their basic molecular properties, including, but not limited to: molecular weight, LogP, number of hydrogen bond acceptors/donors, and number of rotatable bonds. A machine learning model trained on a partition of a dataset exhibiting decoy bias may trivially discriminate ligands based on their molecular properties and, thus, still perform well on an unseen partition of the dataset. Arguably, such a model may not learn any meaningful information about protein-ligand interaction that would allow it to generalise well to a different dataset or in a real-life application. To address this issue, the DUD-E database[46] has been introduced, which uses carefully selected decoys with similar physicochemical properties to the active compounds. Yet, several reports show that both analogue and decoy biases are still present in DUD-E, and as a result, simple baselines often perform competitively to sophisticated algorithms Chen et al.[37], Gabel et al.[71]. For that reason, many research groups suggest adopting a database splitting validation strategy[35], whereby DUD-E is only used to evaluate the performance of models trained on different dataset(s)[36,37]. The database splitting validation strategy[35] is based on the assumption that analogue and decoy biases existing in a training dataset are unlikely to be shared with a test dataset, provided that the two sets have been constructed using distinct inclusion and filtering criteria. In our study, we follow this strategy and use the PDBbind and DUD-E databases for model training and evaluation, respectively. An alternative strategy is to cluster target proteins according to some similarity metric, for example, sequence or structural similarity, and evaluate performance on "unseen" targets only[20,72]. Although this task is more challenging than database splitting, it may not necessarily be more representative of real-life situations, as it is not unreasonable to expect that for some target proteins in the test (i.e., screening) set, one or more similar proteins may exist in the training set.

In addition to using separate datasets for model training and evaluation, a common strategy to quantify the effect of dataset bias on performance is to develop appropriate

baselines. One such example concerns models that ignore the protein or ligand structure altogether[36,37]. To that end, we train a baseline model using ligand data only on the PDBbind refined set, which is the same dataset used to train all machine learning and hybrid docking/machine learning-based models in the benchmark. We observe that our ligand baseline achieves higher than chance-level performance (i.e., $AUROC > 0.5$). This indicates that despite using different datasets for training and testing, discovered biases can to some degree be transferred across datasets. To our knowledge, this finding has not been previously reported and warrants further investigation in future. Interestingly, our ligand baseline performs competitively to many methods in our benchmark. Of note, DeepDTA, RF-score and NN-score show comparable performance to the baseline in terms of EF_1 score (Figure 3 and Table 4). This is somewhat surprising, especially when considering that DeepDTA is regarded as a state-of-the-art method for sequence-based virtual screening[34,58,76]. Overall, our findings further reinforce the need for rigorous evaluation of machine learning models with appropriate baselines.

Virtual screening evaluation metrics

As a final note, we observe a relative discrepancy between the three metrics that we use in our study, namely, AUROC and EF_1 and $BEDROC_{80.5}$ (Table 4). Although these three metrics seem to be positively correlated, their correlation is not very strong (i.e., $r \leq 0.80$, Figure 7). From a statistical perspective, the EF measures recall (i.e., true positive rate), whereas AUROC and BEDROC consider both recall and fall-out (i.e., false positive rate). Furthermore, AUROC and BEDROC are global metrics, although the latter uses different weights for each ligand in the screening library based on its final ranking.

On the other hand, EF_1 only considers the top 1% of ranked ligands for a given target (Figure 7). For virtual screening applications, it can be argued that the EF metric is more relevant, as it is desirable to experimentally validate only a fraction of the top-identified ligands for a given target[47] and also put more emphasis on sensitivity/recall. Despite that

the EF metric may seem more relevant for virtual screening applications, it suffers from its own limitations. Firstly, due to normalising by the total number of true binders for a given target (Equation 4), comparison across datasets, or even targets with the same dataset with different numbers of binders, may not be meaningful[4]. In such cases, the AUROC and BEDROC metric may be more appropriate. The normalisation factor also gives rise to a second limitation. For targets with small numbers of true binders, this metric can become heavily quantised. Nonetheless, the DUD-E database comprises a relatively large amount of active and decoy compounds for each target and therefore the quantisation effect is minimal.

Conclusion

In this work, we propose an end-to-end pipeline for high-throughput SBVS using ensemble GNNs and multiple levels of target protein pocket representation. By explicitly bypassing the requirement for docking simulations, our method achieves comparable performance to several state-of-the-art docking-based and hybrid docking/machine learning-based methods, yet with several orders of magnitude faster screening times. When compared to a purely machine learning-based sequence-level model with comparable inference times, our method achieves remarkably superior performance. In the future, we shall explore extensions of our model and further validate its performance with additional benchmark datasets.

Data and software availability

We provide data and scripts required to reproduce all figures and tables in our manuscript and supplementary material. Additionally, we provide support for using our methodology and trained models for virtual screening via a REST API: https://github.com/deeplab-ai/denvis.

We use the following publicly available datasets: TOUGH-M1, https://osf.io/6ngbs/; PDBbind v.2019, http://www.pdbbind-cn.org/; and DUD-E, http://dude.docking.org/.

Virtual screening results for DUD-E using GNINA, Vina, RF-score nd NN-score are provided from the Koes research group at the Department of Computational and Systems Biology, University of Pittsburgh, and can be found in the following links: AutoDock Vina, http://bits.csb.pitt.edu/files/docked_dude.tar; GNINA, http://bits.csb.pitt.edu/files/defaultCNN_dude.tar.gz; RF-score and NN-score, http://bits.csb.pitt.edu/files/rfnn_dude_scores.tgz.

Conflict of interest disclosure

A.K., N.A., V.P. and S.T. have filed non-provisional patent application PCT/EP2021/084447 in the name of Deeplab IKE relating to machine learning for efficient protein-ligand virtual screening.

Acknowledgement

The authors would like to thank Liliane Mouawad from Curie Institute, Paris for kindly providing screening results for DUD-E with the four docking algorithms (i.e., Gold, Glide, Surflex and FlexX). We are also grateful to David Koes and Jocelyn Sunseri for kindly providing screening results for DUD-E with AutoDock Vina, GNINA, RF-score, and NN-score. We also thank Alexandros Pittis from the European Molecular Biology Laboratory (EMBL) for providing feedback on an earlier version of the manuscript. Finally, we thank NVIDIA Corporation for supporting this research by donating hardware via the "Applied Research Accelerator Program". The authors received no specific funding for this work.

References

(1) DiMasi, J. A.; Grabowski, H. G.; Hansen, R. W. Innovation in the pharmaceutical industry: new estimates of R&D costs. *Journal of health economics* **2016**, *47*, 20–33.

(2) Vamathevan, J.; Clark, D.; Czodrowski, P.; Dunham, I.; Ferran, E.; Lee, G.; Li, B.; Madabhushi, A.; Shah, P.; Spitzer, M., et al. Applications of machine learning in drug discovery and development. *Nature Reviews Drug Discovery* **2019**, *18*, 463–477.

(3) Pushpakom, S.; Iorio, F.; Eyers, P. A.; Escott, K. J.; Hopper, S.; Wells, A.; Doig, A.; Guilliams, T.; Latimer, J.; McNamee, C., et al. Drug repurposing: progress, challenges and recommendations. *Nature reviews Drug discovery* **2019**, *18*, 41–58.

(4) Maia, E. H. B.; Assis, L. C.; de Oliveira, T. A.; da Silva, A. M.; Taranto, A. G. Structure-based virtual screening: From classical to artificial intelligence. *Frontiers in chemistry* **2020**, *8*.

(5) Joint European Disruptive Initiative, Billion molecules against COVID-19 Grand Challenge. https://www.jedi.foundation/billion-molecules, 2020; [Online; accessed October 13, 2021].

(6) Lyne, P. D. Structure-based virtual screening: an overview. *Drug discovery today* **2002**, *7*, 1047–1055.

(7) Banegas-Luna, A.-J.; Cerón-Carrasco, J. P.; Pérez-Sánchez, H. A review of ligand-based virtual screening web tools and screening algorithms in large molecular databases in the age of big data. *Future medicinal chemistry* **2018**, *10*, 2641–2658.

(8) Grinter, S. Z.; Zou, X. Challenges, applications, and recent advances of protein-ligand docking in structure-based drug design. *Molecules* **2014**, *19*, 10150–10176.

(9) Verdonk, M. L.; Cole, J. C.; Hartshorn, M. J.; Murray, C. W.; Taylor, R. D. Improved protein–ligand docking using GOLD. *Proteins: Structure, Function, and Bioinformatics* **2003**, *52*, 609–623.

(10) Jain, A. N. Surflex: fully automatic flexible molecular docking using a molecular similarity-based search engine. *Journal of medicinal chemistry* **2003**, *46*, 499–511.

(11) Halgren, T. A.; Murphy, R. B.; Friesner, R. A.; Beard, H. S.; Frye, L. L.; Pollard, W. T.; Banks, J. L. Glide: a new approach for rapid, accurate docking and scoring. 2. Enrichment factors in database screening. *Journal of medicinal chemistry* **2004**, *47*, 1750–1759.

(12) Schellhammer, I.; Rarey, M. FlexX-Scan: Fast, structure-based virtual screening. *PROTEINS: Structure, Function, and Bioinformatics* **2004**, *57*, 504–517.

(13) Ballester, P. J.; Mitchell, J. B. A machine learning approach to predicting protein–ligand binding affinity with applications to molecular docking. *Bioinformatics* **2010**, *26*, 1169–1175.

(14) Durrant, J. D.; McCammon, J. A. NNScore 2.0: a neural-network receptor–ligand scoring function. *Journal of chemical information and modeling* **2011**, *51*, 2897–2903.

(15) Gomes, J.; Ramsundar, B.; Feinberg, E. N.; Pande, V. S. Atomic convolutional networks for predicting protein-ligand binding affinity. *arXiv:1703.10603* **2017**,

(16) Ragoza, M.; Hochuli, J.; Idrobo, E.; Sunseri, J.; Koes, D. R. Protein–ligand scoring with convolutional neural networks. *Journal of chemical information and modeling* **2017**, *57*, 942–957.

(17) Jiménez, J.; Skalic, M.; Martinez-Rosell, G.; De Fabritiis, G. KDEEP: protein–ligand absolute binding affinity prediction via 3D-convolutional neural networks. *Journal of chemical information and modeling* **2018**, *58*, 287–296.

(18) Imrie, F.; Bradley, A. R.; van der Schaar, M.; Deane, C. M. Protein family-specific models using deep neural networks and transfer learning improve virtual screening and highlight the need for more data. *Journal of chemical information and modeling* **2018**, *58*, 2319–2330.

(19) Zheng, L.; Fan, J.; Mu, Y. Onionnet: a multiple-layer intermolecular-contact-based

convolutional neural network for protein–ligand binding affinity prediction. *ACS omega* **2019**, *4*, 15956–15965.

(20) Francoeur, P. G.; Masuda, T.; Sunseri, J.; Jia, A.; Iovanisci, R. B.; Snyder, I.; Koes, D. R. Three-Dimensional Convolutional Neural Networks and a Cross-Docked Data Set for Structure-Based Drug Design. *Journal of Chemical Information and Modeling* **2020**, *60*, 4200–4215.

(21) McNutt, A. T.; Francoeur, P.; Aggarwal, R.; Masuda, T.; Meli, R.; Ragoza, M.; Sunseri, J.; Koes, D. R. GNINA 1.0: molecular docking with deep learning. *Journal of cheminformatics* **2021**, *13*, 1–20.

(22) Feinberg, E. N.; Sur, D.; Wu, Z.; Husic, B. E.; Mai, H.; Li, Y.; Sun, S.; Yang, J.; Ramsundar, B.; Pande, V. S. PotentialNet for molecular property prediction. *ACS central science* **2018**, *4*, 1520–1530.

(23) Torng, W.; Altman, R. B. Graph convolutional neural networks for predicting drug-target interactions. *Journal of chemical information and modeling* **2019**, *59*, 4131–4149.

(24) Wang, X.; Li, Z.; Jiang, M.; Wang, S.; Zhang, S.; Wei, Z. Molecule property prediction based on spatial graph embedding. *Journal of chemical information and modeling* **2019**, *59*, 3817–3828.

(25) Morrone, J. A.; Weber, J. K.; Huynh, T.; Luo, H.; Cornell, W. D. Combining docking pose rank and structure with deep learning improves protein–ligand binding mode prediction over a baseline docking approach. *Journal of chemical information and modeling* **2020**, *60*, 4170–4179.

(26) Glaser, J.; Vermaas, J. V.; Rogers, D. M.; Larkin, J.; LeGrand, S.; Boehm, S.; Baker, M. B.; Scheinberg, A.; Tillack, A. F.; Thavappiragasam, M., et al. High-throughput virtual laboratory for drug discovery using massive datasets. *The International Journal of High Performance Computing Applications* **2021**, 10943420211001565.

(27) Öztürk, H.; Özgür, A.; Ozkirimli, E. DeepDTA: deep drug–target binding affinity prediction. *Bioinformatics* **2018**, *34*, i821–i829.

(28) Öztürk, H.; Ozkirimli, E.; Özgür, A. WideDTA: prediction of drug-target binding affinity. *arXiv:1902.04166* **2019**,

(29) Feng, Q.; Dueva, E.; Cherkasov, A.; Ester, M. PADME: A deep learning-based framework for drug-target interaction prediction. *arXiv:1807.09741* **2018**,

(30) Lee, I.; Keum, J.; Nam, H. DeepConv-DTI: prediction of drug-target interactions via deep learning with convolution on protein sequences. *PLoS computational biology* **2019**, *15*, e1007129.

(31) Karimi, M.; Wu, D.; Wang, Z.; Shen, Y. DeepAffinity: interpretable deep learning of compound–protein affinity through unified recurrent and convolutional neural networks. *Bioinformatics* **2019**, *35*, 3329–3338.

(32) Nguyen, T.; Le, H.; Quinn, T. P.; Nguyen, T.; Le, T. D.; Venkatesh, S. GraphDTA: predicting drug–target binding affinity with graph neural networks. *Bioinformatics* **2020**,

(33) Jiang, M.; Li, Z.; Zhang, S.; Wang, S.; Wang, X.; Yuan, Q.; Wei, Z. Drug–target affinity prediction using graph neural network and contact maps. *RSC Advances* **2020**, *10*, 20701–20712.

(34) Li, S.; Wan, F.; Shu, H.; Jiang, T.; Zhao, D.; Zeng, J. MONN: a multi-objective neural network for predicting compound-protein interactions and affinities. *Cell Systems* **2020**, *10*, 308–322.

(35) Lopez-del Rio, A.; Nonell-Canals, A.; Vidal, D.; Perera-Lluna, A. Evaluation of cross-validation strategies in sequence-based binding prediction using deep learning. *Journal of chemical information and modeling* **2019**, *59*, 1645–1657.

(36) Yang, J.; Shen, C.; Huang, N. Predicting or pretending: artificial intelligence for protein-ligand interactions lack of sufficiently large and unbiased datasets. *Frontiers in pharmacology* **2020**, *11*, 69.

(37) Chen, L.; Cruz, A.; Ramsey, S.; Dickson, C. J.; Duca, J. S.; Hornak, V.; Koes, D. R.; Kurtzman, T. Hidden bias in the DUD-E dataset leads to misleading performance of deep learning in structure-based virtual screening. *PloS one* **2019**, *14*, e0220113.

(38) Xu, K.; Hu, W.; Leskovec, J.; Jegelka, S. How powerful are graph neural networks? *arXiv:1810.00826* **2018**,

(39) Hu, W.; Liu, B.; Gomes, J.; Zitnik, M.; Liang, P.; Pande, V.; Leskovec, J. Strategies for pre-training graph neural networks. *arXiv preprint arXiv:1905.12265* **2019**,

(40) Hu, W.; Fey, M.; Zitnik, M.; Dong, Y.; Ren, H.; Liu, B.; Catasta, M.; Leskovec, J. Open Graph benchmark: Datasets for machine learning on graphs. *arXiv preprint arXiv:2005.00687* **2020**,

(41) Monti, F.; Boscaini, D.; Masci, J.; Rodola, E.; Svoboda, J.; Bronstein, M. M. Geometric deep learning on graphs and manifolds using mixture model CNNs. Proceedings of the IEEE conference on computer vision and pattern recognition. 2017; pp 5115–5124.

(42) Gainza, P.; Sverrisson, F.; Monti, F.; Rodola, E.; Boscaini, D.; Bronstein, M.; Correia, B. Deciphering interaction fingerprints from protein molecular surfaces using geometric deep learning. *Nature Methods* **2020**, *17*, 184–192.

(43) Sehnal, D.; Rose, A.; Koca, J.; Burley, S.; Velankar, S. Mol*: towards a common library and tools for web molecular graphics. Workshop on molecular graphics and visual analysis of molecular data. 2018.

(44) Govindaraj, R. G.; Brylinski, M. Comparative assessment of strategies to identify similar ligand-binding pockets in proteins. *BMC bioinformatics* **2018**, *19*, 1–17.

(45) Liu, Z.; Su, M.; Han, L.; Liu, J.; Yang, Q.; Li, Y.; Wang, R. Forging the basis for developing protein–ligand interaction scoring functions. *Accounts of chemical research* **2017**, *50*, 302–309.

(46) Mysinger, M. M.; Carchia, M.; Irwin, J. J.; Shoichet, B. K. Directory of useful decoys, enhanced (DUD-E): better ligands and decoys for better benchmarking. *Journal of medicinal chemistry* **2012**, *55*, 6582–6594.

(47) Su, M.; Yang, Q.; Du, Y.; Feng, G.; Liu, Z.; Li, Y.; Wang, R. Comparative assessment of scoring functions: the CASF-2016 update. *Journal of chemical information and modeling* **2018**, *59*, 895–913.

(48) Wang, R.; Fang, X.; Lu, Y.; Yang, C.-Y.; Wang, S. The PDBbind database: methodologies and updates. *Journal of medicinal chemistry* **2005**, *48*, 4111–4119.

(49) Le Guilloux, V.; Schmidtke, P.; Tuffery, P. Fpocket: an open source platform for ligand pocket detection. *BMC bioinformatics* **2009**, *10*, 1–11.

(50) Howard, J.; Gugger, S. Fastai: A layered API for deep learning. *Information* **2020**, *11*, 108.

(51) Bromley, J.; Guyon, I.; LeCun, Y.; Säckinger, E.; Shah, R. Signature verification using a" siamese" time delay neural network. *Advances in neural information processing systems* **1993**, *6*, 737–744.

(52) Chen, T.; Kornblith, S.; Norouzi, M.; Hinton, G. A simple framework for contrastive learning of visual representations. International conference on machine learning. 2020; pp 1597–1607.

(53) Yung-Chi, C.; Prusoff, W. H. Relationship between the inhibition constant (KI) and the concentration of inhibitor which causes 50 per cent inhibition (I50) of an enzymatic reaction. *Biochemical pharmacology* **1973**, *22*, 3099–3108.

(54) Truchon, J.-F.; Bayly, C. I. Evaluating virtual screening methods: good and bad metrics for the "early recognition" problem. *Journal of chemical information and modeling* **2007**, *47*, 488–508.

(55) Chaput, L.; Martinez-Sanz, J.; Saettel, N.; Mouawad, L. Benchmark of four popular virtual screening programs: construction of the active/decoy dataset remains a major determinant of measured performance. *Journal of cheminformatics* **2016**, *8*, 1–17.

(56) Su, M.; Yang, Q.; Du, Y.; Feng, G.; Liu, Z.; Li, Y.; Wang, R. Comparative assessment of scoring functions: the CASF-2016 update. *Journal of chemical information and modeling* **2018**, *59*, 895–913.

(57) Trott, O.; Olson, A. J. AutoDock Vina: improving the speed and accuracy of docking with a new scoring function, efficient optimization, and multithreading. *Journal of computational chemistry* **2010**, *31*, 455–461.

(58) Huang, K.; Fu, T.; Xiao, C.; Glass, L.; Sun, J. DeepPurpose: a deep learning based drug repurposing toolkit. *arXiv:2004.08919* **2020**,

(59) Davis, M. I.; Hunt, J. P.; Herrgard, S.; Ciceri, P.; Wodicka, L. M.; Pallares, G.; Hocker, M.; Treiber, D. K.; Zarrinkar, P. P. Comprehensive analysis of kinase inhibitor selectivity. *Nature biotechnology* **2011**, *29*, 1046–1051.

(60) Sieg, J.; Flachsenberg, F.; Rarey, M. In need of bias control: evaluating chemical data for machine learning in structure-based virtual screening. *Journal of chemical information and modeling* **2019**, *59*, 947–961.

(61) Cambridge Crystallographic Data Centre, Ultra-large docking. How to run ultra-large GOLD docking jobs on cloud resources. https://usermanual.wiki/m/5735088be183d28de5426de0958420824caa4c41194d6fe088ee2a48deebed21.pdf, 2020; [Online; accessed October 13, 2021].

(62) BioSolveIT, FlexX-docking. https://www.biosolveit.de/wp-content/uploads/2021/01/FlexX.pdf, 2021; [Online; accessed October 13, 2021].

(63) BioPharmics LLC, Surflex Platform Manual. https://www.biopharmics.com/Public/Surflex-Manual.pdf, 2021; [Online; accessed October 13, 2021].

(64) Schrödinger, Glide Knowledge base. https://www.schrodinger.com/kb/1012, 2020; [Online; accessed October 13, 2021].

(65) Méndez-Lucio, O.; Ahmad, M.; del Rio-Chanona, E. A.; Wegner, J. K. A geometric deep learning approach to predict binding conformations of bioactive molecules. **2021**,

(66) Houston, D. R.; Walkinshaw, M. D. Consensus docking: improving the reliability of docking in a virtual screening context. *Journal of chemical information and modeling* **2013**, *53*, 384–390.

(67) Stokes, J. M.; Yang, K.; Swanson, K.; Jin, W.; Cubillos-Ruiz, A.; Donghia, N. M.; MacNair, C. R.; French, S.; Carfrae, L. A.; Bloom-Ackermann, Z., et al. A deep learning approach to antibiotic discovery. *Cell* **2020**, *180*, 688–702.

(68) Hinton, G.; Vinyals, O.; Dean, J. Distilling the knowledge in a neural network. *arXiv:1503.02531* **2015**,

(69) Allen-Zhu, Z.; Li, Y. Towards understanding ensemble, knowledge distillation and self-distillation in deep learning. *arXiv preprint arXiv:2012.09816* **2020**,

(70) Kramer, C.; Gedeck, P. Leave-cluster-out cross-validation is appropriate for scoring functions derived from diverse protein data sets. *Journal of chemical information and modeling* **2010**, *50*, 1961–1969.

(71) Gabel, J.; Desaphy, J.; Rognan, D. Beware of machine learning-based scoring functions—on the danger of developing black boxes. *Journal of chemical information and modeling* **2014**, *54*, 2807–2815.

(72) Li, Y.; Yang, J. Structural and sequence similarity makes a significant impact on machine-learning-based scoring functions for protein–ligand interactions. *Journal of chemical information and modeling* **2017**, *57*, 1007–1012.

(73) Wallach, I.; Heifets, A. Most ligand-based classification benchmarks reward memorization rather than generalization. *Journal of chemical information and modeling* **2018**, *58*, 916–932.

(74) Cheng, T.; Li, X.; Li, Y.; Liu, Z.; Wang, R. Comparative assessment of scoring functions on a diverse test set. *Journal of chemical information and modeling* **2009**, *49*, 1079–1093.

(75) Good, A. C.; Oprea, T. I. Optimization of CAMD techniques 3. Virtual screening enrichment studies: a help or hindrance in tool selection? *Journal of computer-aided molecular design* **2008**, *22*, 169–178.

(76) Thafar, M.; Raies, A. B.; Albaradei, S.; Essack, M.; Bajic, V. B. Comparison study of computational prediction tools for drug-target binding affinities. *Frontiers in chemistry* **2019**, *7*, 782.

Supplementary Material

DENVIS: scalable and high-throughput virtual screening using graph neural networks with atomic and surface protein pocket features

Agamemnon Krasoulis,[*,†,‡] Nick Antonopoulos,[†,‡] Vassilis Pitsikalis,[†] and Stavros Theodorakis[†]

†*DeepLab, Leoforos Syngrou 106, Athens, Greece*

‡*Contributed equally to this work*

E-mail: a.krasoulis@deeplab.ai

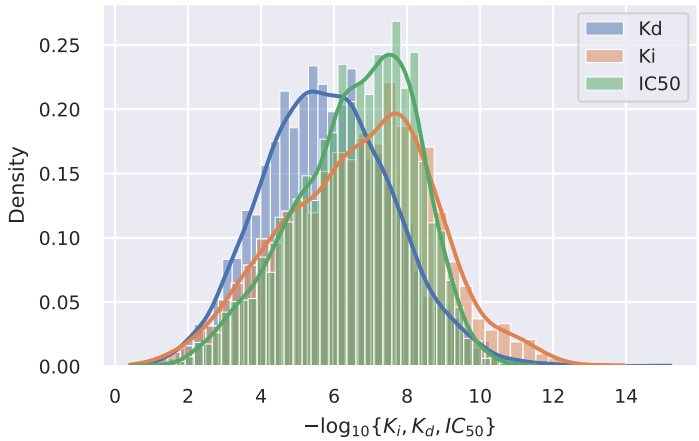

Figure S1: Empirical distributions of the three binding affinity metrics in PDBbind general set: K_i, K_d and IC_{50}. Normalised histograms are shown along with kernel density estimates using Gaussian kernels.

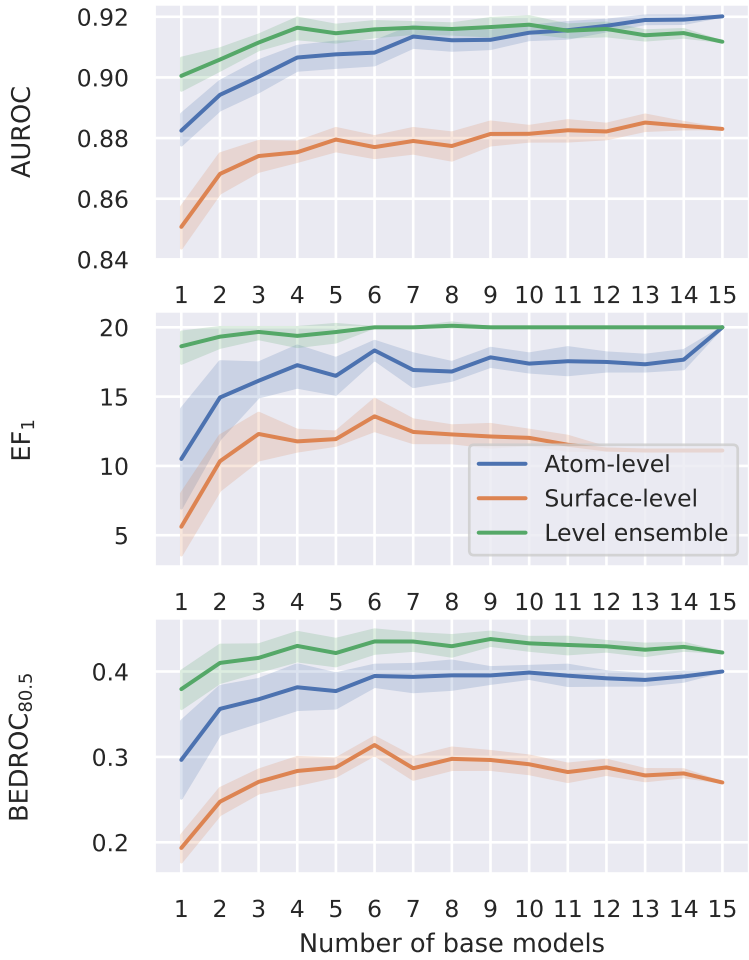

Figure S2: Performance against number of base models in ensembles. Performance is measured on the CASF-2016 benchmark (i.e., PDBBind core set v.2019). A total of 15 atom-level and surface-level models are independently trained on PDBbind refined set. To obtain confidence intervals, twenty independent runs are simulated. In each run, and for each number of base models in the horizontal axis, a subset of the 15 totally available models is sampled without replacement and the average (i.e., median) performance across targets is computed. Confidence intervals are not estimated for $n_{models} = 15$.

	D-G	D-R	DDTA	Gold	Glide	Surflex	Flexx	Vina	GNINA	RF	NN	Bsl.
aa2ar	0.84	0.43	0.59	0.87	0.80	0.77	0.74	0.65	0.74	0.50	0.54	0.57
abl1	0.89	0.90	0.65	0.90	0.74	0.76	0.85	0.78	0.79	0.68	0.62	0.81
ace	0.90	0.96	0.41	0.74	0.72	0.77	0.61	0.56	0.61	0.67	0.75	0.40
aces	0.81	0.82	0.62	0.75	0.67	0.73	0.57	0.78	0.62	0.66	0.65	0.67
ada	0.99	0.99	0.61	0.91	0.68	0.83	0.55	0.57	0.76	0.61	0.58	0.61
ada17	0.99	0.98	0.50	0.77	0.81	0.92	0.60	0.71	0.82	0.66	0.69	0.70
adrb1	0.90	0.62	0.54	0.86	0.88	0.80	0.76	0.73	0.63	0.68	0.58	0.34
adrb2	0.89	0.64	0.56	0.87	0.88	0.81	0.84	0.71	0.71	0.62	0.61	0.35
akt1	0.88	0.96	0.79	0.91	0.78	0.63	0.73	0.76	0.76	0.63	0.49	0.71
akt2	0.87	0.91	0.72	0.94	0.85	0.77	0.86	0.79	0.81	0.56	0.65	0.65
aldr	0.56	0.60	0.45	0.79	0.79	0.65	0.74	0.74	0.56	0.59	0.50	0.55
ampc	0.86	0.86	0.46	0.75	0.79	0.49	0.67	0.61	0.52	0.34	0.57	0.26
andr	0.94	0.88	0.57	0.57	0.84	0.57	0.41	0.63	0.79	0.64	0.57	0.69
aofb	0.58	0.54	0.47	0.84	0.76	0.68	0.71	0.78	0.51	0.53	0.56	0.54
bace1	0.94	0.85	0.66	0.78	0.82	0.80	0.76	0.72	0.82	0.79	0.63	0.61
braf	0.96	0.95	0.67	0.91	0.86	0.70	0.89	0.86	0.83	0.63	0.56	0.80
cah2	0.97	0.94	0.75	0.82	0.77	0.64	0.73	0.59	0.93	0.82	0.68	0.76
casp3	0.92	0.63	0.53	0.91	0.76	0.70	0.70	0.70	0.65	0.54	0.63	0.51
cdk2	0.96	0.90	0.66	0.85	0.88	0.64	0.76	0.72	0.80	0.55	0.59	0.77
comt	0.98	0.58	0.48	0.99	1.00	0.75	0.66	0.63	0.65	0.27	0.42	0.37
cp2c9	0.56	0.55	0.57	0.82	0.64	0.59	0.70	0.62	0.62	0.59	0.53	0.58
cp3a4	0.41	0.43	0.61	0.77	0.72	0.61	0.60	0.60	0.66	0.58	0.51	0.62
csf1r	0.97	0.91	0.74	0.87	0.80	0.61	0.84	0.69	0.78	NaN	NaN	0.80
cxcr4	0.78	0.77	0.52	0.92	0.72	0.76	0.47	0.60	0.85	0.68	0.80	0.71
def	1.00	0.96	0.48	0.91	0.87	0.93	0.70	0.76	0.93	0.60	0.56	0.54
dhi1	0.33	0.52	0.56	0.75	0.68	0.74	0.49	0.77	0.72	0.62	0.68	0.59
dpp4	0.93	0.78	0.71	0.75	0.87	0.71	0.86	0.62	0.75	0.60	0.67	0.62
drd3	0.56	0.55	0.55	0.73	0.72	0.77	0.67	0.75	0.71	0.66	0.60	0.66
dyr	0.96	0.94	0.61	0.92	0.87	0.87	0.67	0.77	0.90	0.55	0.68	0.67
egfr	0.93	0.91	0.58	0.84	0.84	0.67	0.83	0.64	0.77	0.54	0.55	0.69
esr1	0.97	0.79	0.56	0.76	0.91	0.76	0.80	0.83	0.80	0.64	0.50	0.71
esr2	0.93	0.75	0.55	0.79	0.94	0.76	0.84	0.80	0.79	0.65	0.50	0.71
fa10	0.96	0.88	0.71	0.90	0.68	0.78	0.88	0.83	0.88	0.80	0.55	0.72
fa7	0.99	0.99	0.67	0.97	0.91	0.98	0.97	0.91	0.91	0.85	0.70	0.55
fabp4	0.95	0.90	0.53	0.87	0.85	0.76	0.87	0.78	0.53	0.66	0.30	0.44
fak1	0.99	0.99	0.56	0.95	0.80	0.64	0.88	0.81	0.84	0.70	0.49	0.88
fgfr1	0.47	0.56	0.53	0.70	0.48	0.58	0.59	NaN	0.94	NaN	NaN	0.49
fkb1a	0.95	0.89	0.40	0.84	0.87	0.80	0.58	0.77	0.78	0.65	0.57	0.47
fnta	0.90	0.74	0.58	0.78	0.75	0.69	0.76	0.65	0.78	0.74	0.57	0.73
fpps	0.74	0.71	0.20	1.00	0.55	0.52	0.82	0.29	0.98	0.20	1.00	0.32
gcr	0.69	0.80	0.64	0.54	0.72	0.67	0.54	0.64	0.75	0.60	0.64	0.75
glcm	0.72	0.68	0.48	0.90	0.65	0.82	0.69	0.49	0.58	0.49	0.60	0.49
gria2	0.67	0.72	0.67	0.83	0.77	0.75	0.76	0.75	0.83	0.56	0.62	0.60
grik1	0.90	0.84	0.60	0.92	0.90	0.81	0.87	0.59	0.73	0.46	0.68	0.50
hdac2	0.96	0.92	0.61	0.88	0.63	0.85	0.81	0.85	0.80	0.81	0.54	0.75
hdac8	0.98	0.94	0.60	0.87	0.88	0.84	0.76	0.82	0.83	0.75	0.53	0.77
hivint	0.47	0.44	0.44	0.78	0.72	0.67	0.67	0.71	0.50	0.48	0.47	0.52
hivpr	0.94	0.92	0.51	0.64	0.72	0.82	0.55	0.72	0.85	0.77	0.58	0.65
hivrt	0.84	0.58	0.45	0.80	0.83	0.67	0.61	0.68	0.82	0.50	0.56	0.56
hmdh	0.87	0.85	0.57	0.87	0.92	0.83	0.67	0.79	0.92	0.71	0.69	0.66
hs90a	0.99	0.89	0.57	0.85	0.65	0.49	0.34	0.26	0.73	0.39	0.44	0.52
hxk4	0.84	0.78	0.54	0.88	0.57	0.56	0.67	0.57	0.82	0.62	0.63	0.74
igf1r	0.94	0.93	0.68	0.90	0.86	0.70	0.89	0.83	0.85	0.57	0.62	0.76
inha	0.86	0.62	0.38	0.96	0.56	0.84	0.69	0.72	0.68	0.66	0.54	0.57
ital	0.89	0.65	0.47	0.80	0.68	0.50	0.61	0.60	0.66	0.61	0.48	0.76
jak2	0.99	0.94	0.70	0.94	0.88	0.73	0.83	0.78	0.91	0.51	0.63	0.84
kif11	0.81	0.73	0.54	0.89	0.90	0.70	0.69	0.85	0.81	0.72	0.54	0.70
kit	0.96	0.96	0.67	0.83	0.65	0.60	0.79	0.78	0.79	0.65	0.56	0.74
kith	0.28	0.38	0.36	0.87	0.72	0.83	0.82	0.74	0.73	0.57	0.67	0.30
kpcb	0.82	0.78	0.59	0.90	0.86	0.84	0.80	0.77	0.71	0.69	0.49	0.60
lck	0.91	0.94	0.64	0.80	0.83	0.72	0.84	0.80	0.76	0.49	0.53	0.79
lkha4	0.99	0.95	0.52	0.85	0.94	0.90	0.83	0.89	0.88	0.63	0.35	0.58
mapk2	0.95	0.92	0.75	0.91	0.92	0.68	0.81	0.89	0.90	0.64	0.54	0.80
mcr	0.92	0.79	0.61	0.54	0.82	0.55	0.41	0.54	0.84	0.72	0.70	0.72
met	0.92	0.94	0.65	0.93	0.83	0.72	0.82	0.81	0.88	0.74	0.59	0.78
mk01	0.97	0.96	0.65	0.94	0.84	0.74	0.87	0.86	0.76	0.68	0.61	0.83
mk10	0.95	0.89	0.66	0.91	0.85	0.61	0.78	0.75	0.81	0.56	0.57	0.81
mk14	0.98	0.91	0.71	0.82	0.72	0.55	0.85	0.74	0.75	0.64	0.51	0.81
mmp13	1.00	0.97	0.57	0.76	0.77	0.83	0.63	0.66	0.75	0.66	0.63	0.84
mp2k1	0.81	0.73	0.55	0.86	0.75	0.59	0.81	0.54	0.70	0.56	0.68	0.67
nos1	0.41	0.60	0.47	0.87	0.75	0.72	0.76	0.59	0.64	0.54	0.60	0.45
nram	0.98	0.96	0.33	0.93	0.95	0.92	0.82	0.54	0.94	0.57	0.60	0.32
pa2ga	0.91	0.84	0.53	0.82	0.79	0.72	0.72	0.62	0.81	0.62	0.41	0.49
parp1	0.92	0.86	0.64	0.80	0.95	0.79	0.84	0.86	0.87	0.58	0.62	0.66
pde5a	0.89	0.80	0.65	0.73	0.85	0.69	0.65	0.66	0.81	0.58	0.62	0.65
pgh1	0.21	0.39	0.54	0.73	0.76	0.68	0.63	0.64	0.67	0.56	0.46	0.68
pgh2	0.45	0.57	0.65	0.77	0.82	0.76	0.75	0.77	0.75	0.57	0.46	0.76
plk1	0.93	0.94	0.60	0.90	0.91	0.62	0.81	0.64	0.91	0.60	0.47	0.63
pnph	1.00	0.99	0.83	0.94	0.76	0.68	0.74	0.88	0.91	0.52	0.59	0.76
ppara	0.95	0.87	0.50	0.85	0.73	0.86	0.75	0.86	0.76	0.62	0.54	0.57
ppard	0.96	0.93	0.52	0.84	0.66	0.85	0.68	0.76	0.74	0.54	0.51	0.58
pparg	0.92	0.84	0.51	0.84	0.74	0.79	0.67	0.79	0.74	0.71	0.53	0.61
prgr	0.90	0.82	0.62	0.64	0.84	0.63	0.68	0.67	0.80	0.67	0.65	0.79
ptn1	0.76	0.62	0.58	0.91	0.84	0.85	0.82	0.83	0.81	0.62	0.60	0.65

pur2	1.00	0.94	0.87	1.00	0.99	1.00	1.00	0.91	1.00	0.74	0.83	0.75
pygm	0.62	0.43	0.42	0.80	0.56	0.55	0.74	0.60	0.51	0.62	0.67	0.55
pyrd	0.59	0.67	0.53	0.85	0.88	0.77	0.83	0.83	0.73	0.78	0.49	0.73
reni	0.83	0.74	0.62	0.85	0.84	0.90	0.73	0.66	0.75	0.71	0.65	0.48
rock1	0.88	0.83	0.65	0.90	0.84	0.74	0.91	0.72	0.85	0.57	0.55	0.69
rxra	0.95	0.94	0.65	0.82	0.97	0.84	0.80	0.81	0.93	0.47	0.52	0.93
sahh	0.90	0.84	0.32	0.89	0.98	0.91	0.91	0.80	0.75	0.54	0.71	0.15
src	0.93	0.93	0.72	0.77	0.74	0.62	0.80	0.65	0.84	0.53	0.55	0.78
tgfr1	0.99	0.94	0.71	0.96	0.96	0.77	0.89	0.90	0.93	0.58	0.49	0.57
thb	0.92	0.71	0.51	0.91	0.85	0.87	0.83	0.82	0.88	0.61	0.38	0.71
thrb	0.99	0.96	0.66	0.85	0.92	0.88	0.88	0.77	0.92	0.81	0.79	0.58
try1	0.98	0.95	0.74	0.88	0.91	0.94	0.90	0.80	0.89	0.78	0.72	0.61
tryb1	0.73	0.87	0.67	0.90	0.88	0.91	0.86	0.71	0.66	0.72	0.66	0.49
tysy	0.89	0.56	0.71	0.94	0.93	0.84	0.84	0.87	0.87	0.68	0.64	0.70
urok	0.98	0.95	0.72	0.91	0.92	0.76	0.93	0.77	0.82	0.67	0.60	0.69
vgfr2	0.82	0.94	0.70	0.82	0.68	0.69	0.85	0.77	0.83	0.71	0.50	0.73
wee1	1.00	0.91	0.49	0.98	1.00	0.95	0.96	0.96	0.96	0.77	0.59	0.78
xiap	0.91	0.89	0.58	0.94	0.82	0.90	0.91	0.73	0.89	0.74	0.80	0.41

Table S1: DUD-E per-target AUROC scores. Abbreviations: D-G, DENVIS-PDBbind general set; D-R, DENVIS-PDBbind refind set; DDTA, Deep DTA; RF, RF-score; NN, NN-score; Bsl., Ligand baseline.

	D-G	D-R	DDTA	Gold	Glide	Surflex	Flexx	Vina	GNINA	RF	NN	Bsl.
aa2ar	35.68	0.21	1.66	17.01	5.21	19.71	6.02	2.49	6.43	2.28	0.62	1.24
abl1	51.65	41.21	8.24	26.92	17.42	17.03	27.78	13.26	20.44	11.05	2.21	4.40
ace	29.08	32.27	0.00	14.54	5.42	2.48	1.42	2.86	4.29	5.71	4.64	0.00
aces	20.97	3.31	8.83	22.52	8.13	20.31	1.35	14.57	15.45	3.97	1.55	3.31
ada	59.14	40.86	0.00	18.28	5.38	9.68	10.75	1.08	13.98	4.30	0.00	0.00
ada17	67.67	65.04	0.56	20.49	28.91	35.90	1.89	28.01	31.58	2.82	3.76	2.07
adrb1	22.27	0.00	2.43	27.53	18.70	15.38	9.35	4.05	4.05	0.40	2.02	0.40
adrb2	30.74	2.16	2.16	26.41	27.71	20.35	20.00	3.46	6.93	0.87	3.46	1.30
akt1	17.75	31.74	4.44	20.48	10.92	4.44	5.17	5.46	4.10	1.37	0.00	1.37
akt2	31.62	12.82	3.42	41.03	24.35	14.53	13.68	26.50	11.11	0.85	1.71	4.27
aldr	5.66	1.89	0.00	23.90	27.67	7.55	11.95	9.43	8.81	1.26	0.00	1.89
ampc	16.67	12.50	0.00	0.00	2.08	0.00	0.00	0.00	2.08	0.00	0.00	0.00
andr	32.71	21.56	1.49	1.12	25.70	4.09	0.00	17.84	8.55	1.49	2.60	2.23
aofb	2.46	0.00	0.82	16.39	6.67	4.92	5.26	6.56	1.64	0.82	0.00	4.92
bace1	50.53	19.43	0.35	25.44	14.13	17.31	11.11	4.59	20.85	18.37	2.12	0.00
braf	46.71	42.76	3.95	25.00	29.80	5.26	23.03	17.11	21.71	12.50	0.66	1.32
cah2	63.62	63.21	1.42	16.70	3.89	3.05	7.39	0.00	26.22	18.50	3.66	14.02
casp3	39.20	0.00	0.00	25.13	27.78	12.56	22.11	1.52	17.17	2.02	4.04	0.00
cdk2	44.51	30.80	2.74	15.82	29.87	3.16	11.80	9.51	21.35	0.85	1.48	9.49
comt	75.61	4.88	0.00	70.73	83.78	2.44	9.76	4.88	0.00	0.00	4.88	0.00
cp2c9	10.00	5.83	1.67	5.83	0.88	3.33	9.09	3.33	5.00	5.00	0.00	0.00
cp3a4	2.94	3.53	3.53	12.35	11.80	8.82	4.19	1.80	1.20	3.59	0.00	2.35
csf1r	43.37	27.11	4.82	19.28	18.40	3.01	24.54	1.20	19.28	NaN	NaN	4.22
cxcr4	30.00	2.50	2.50	2.50	0.00	15.00	0.00	0.00	15.00	0.00	5.00	0.00
def	53.92	48.04	0.00	26.47	5.13	32.35	0.00	9.80	31.37	4.90	1.96	0.00
dhi1	0.00	2.12	1.21	8.79	7.03	3.64	0.63	4.24	10.91	6.36	1.82	1.21
dpp4	30.58	3.38	4.50	20.08	11.84	6.38	11.84	0.56	14.63	0.75	3.19	1.88
drd3	7.92	1.04	1.04	11.04	1.69	7.08	2.51	5.02	8.16	3.77	1.26	4.17
dyr	57.58	50.22	2.60	48.48	30.87	25.54	10.43	7.36	28.57	1.30	1.30	1.73
egfr	62.36	46.49	2.58	25.09	24.95	13.65	19.29	5.72	22.69	2.58	2.77	8.86
esr1	53.26	9.14	2.35	24.61	48.78	27.15	31.73	18.54	24.80	0.00	1.31	0.52
esr2	50.68	11.72	1.91	17.49	44.26	21.80	31.02	14.99	29.16	0.00	0.27	0.82
fa10	31.84	28.86	4.47	34.26	13.74	8.57	33.08	15.83	26.44	13.04	0.93	2.42
fa7	56.14	41.23	3.51	45.61	44.04	42.11	55.26	11.40	30.70	18.42	0.00	0.00
fabp4	48.94	17.02	0.00	31.91	25.58	2.13	17.02	29.79	0.00	0.00	0.00	0.00
fak1	55.00	55.00	2.00	29.00	20.00	5.00	15.00	19.00	27.00	2.00	0.00	3.00
fgfr1	1.44	2.16	2.16	3.60	0.00	0.72	0.76	1.44	42.45	1.44	1.44	1.44
fkb1a	31.53	11.71	0.00	25.00	41.82	9.91	0.00	7.21	3.60	1.80	0.00	0.90
fnta	53.04	2.20	0.84	21.62	6.85	4.94	6.26	2.70	8.45	8.11	1.52	1.18
fpps	0.00	0.00	0.00	91.76	1.23	1.18	1.18	0.00	38.82	0.00	78.82	0.00
gcr	9.30	15.50	0.78	6.98	16.56	15.12	7.63	15.12	15.50	2.33	2.33	3.88
glcm	0.00	3.70	1.85	27.78	11.11	31.48	5.56	0.00	7.41	0.00	1.85	0.00
gria2	13.29	16.46	1.90	14.56	33.33	8.23	7.59	10.76	18.35	4.43	8.86	2.53
grik1	42.57	35.64	0.99	29.70	20.00	6.93	19.80	4.00	12.00	2.00	4.00	0.99
hdac2	55.14	53.51	2.70	16.76	15.84	12.97	16.30	11.89	3.78	2.70	2.16	3.78
hdac8	62.94	60.00	1.76	10.00	2.45	5.29	12.94	20.00	16.47	3.53	0.59	5.29
hivint	0.00	0.00	0.00	9.00	2.06	3.00	4.00	2.00	0.00	0.00	0.00	0.00
hivpr	50.93	18.28	1.49	17.91	9.14	5.04	2.08	4.10	28.36	23.51	0.19	7.09
hivrt	14.20	2.37	0.59	12.72	22.94	4.73	2.08	4.15	11.28	0.30	2.08	6.21
hmdh	45.29	47.06	0.00	24.12	39.41	17.06	1.76	4.12	36.47	4.71	1.76	0.00
hs90a	38.64	15.91	2.27	13.64	1.16	1.14	2.35	0.00	11.36	0.00	2.27	0.00
hxk4	19.57	2.17	1.09	14.13	22.83	0.00	4.35	3.26	20.65	0.00	0.00	14.13
igf1r	51.35	46.62	3.38	28.38	32.65	10.81	27.70	16.22	30.41	12.84	2.70	1.35
inha	20.93	0.00	0.00	25.58	9.30	4.65	9.30	6.98	2.33	0.00	0.00	0.00
ital	44.20	10.87	0.00	6.52	8.91	2.90	1.45	0.00	6.57	0.73	0.73	2.90
jak2	57.01	47.66	6.54	28.97	33.77	14.95	8.41	15.89	28.04	8.41	2.80	7.48
kif11	27.59	16.38	0.00	33.62	38.79	6.03	2.59	24.14	37.93	14.66	0.00	4.31
kit	35.54	30.12	4.22	14.46	6.10	3.01	7.88	4.82	13.86	6.63	2.41	4.22
kith	0.00	0.00	0.00	15.79	30.77	42.11	0.00	33.33	38.60	1.75	0.00	0.00
kpcb	58.52	31.11	0.00	28.89	52.46	27.41	27.48	28.15	23.70	0.00	2.22	6.67
lck	50.24	42.14	3.81	15.48	25.12	13.57	18.12	10.00	15.24	3.57	0.71	2.14
lkha4	52.63	33.92	0.00	13.45	28.24	18.71	7.60	14.71	15.29	0.00	0.00	1.17

mapk2	43.56	25.74	14.85	21.78	27.72	2.97	6.93	13.86	16.83	1.98	1.98	3.96
mcr	27.66	22.34	1.06	2.13	29.41	2.13	0.00	7.45	10.64	4.26	9.57	4.26
met	68.07	58.43	1.20	39.76	27.71	9.04	18.07	12.05	37.95	19.28	1.20	1.20
mk01	59.49	43.04	1.27	20.25	12.66	1.27	21.52	3.80	10.13	5.06	1.27	1.27
mk10	44.23	26.92	3.85	23.08	12.50	3.85	14.42	7.69	7.69	4.81	0.96	4.81
mk14	57.61	27.16	2.42	14.19	22.15	3.29	14.19	6.57	19.38	7.44	0.52	4.84
mmp13	65.56	64.86	1.57	25.70	18.41	12.76	4.20	4.02	9.09	5.59	2.10	9.27
mp2k1	28.10	32.23	0.00	23.14	13.22	0.00	8.33	0.00	5.83	0.83	5.00	6.61
nos1	3.00	1.00	1.00	20.00	14.29	24.00	7.07	2.00	8.00	0.00	2.00	1.00
nram	50.00	41.84	0.00	19.39	41.84	22.45	14.29	0.00	17.35	0.00	0.00	0.00
pa2ga	37.37	20.20	2.02	20.20	35.35	2.02	17.53	1.02	9.18	0.00	0.00	0.00
parp1	36.22	18.50	0.98	14.17	41.12	19.09	12.40	13.78	16.14	2.56	1.18	0.79
pde5a	27.14	13.82	2.76	10.55	21.77	8.79	1.76	11.81	14.32	1.01	1.26	0.50
pgh1	0.00	0.00	3.08	14.36	17.11	7.18	5.21	6.15	9.23	1.54	1.03	9.23
pgh2	0.92	0.00	5.06	18.62	34.91	14.94	11.08	25.98	17.24	1.84	1.38	12.18
plk1	31.78	38.32	0.00	30.84	43.81	3.74	8.41	0.00	38.68	5.66	5.66	0.93
pnph	65.05	63.11	19.42	25.24	7.77	10.68	10.68	11.76	35.29	0.00	1.96	3.88
ppara	50.13	22.25	1.34	17.43	8.94	12.60	3.77	6.70	4.83	0.80	2.14	0.80
ppard	48.75	33.75	3.33	12.08	3.61	10.42	1.25	1.25	4.58	1.25	0.42	1.25
pparg	50.00	6.61	1.24	17.36	7.53	4.96	1.66	6.20	5.99	3.10	1.24	1.03
prgr	22.87	9.90	3.41	2.39	19.05	4.44	3.64	12.97	18.43	2.39	3.75	7.85
ptn1	24.62	18.46	0.77	41.54	15.45	10.77	14.84	26.15	25.38	10.00	4.62	0.00
pur2	56.00	12.00	6.00	56.00	54.00	56.00	56.00	4.00	52.00	0.00	12.00	0.00
pygm	0.00	1.30	1.30	6.49	1.30	0.00	9.09	2.60	3.90	0.00	9.09	0.00
pyrd	0.90	0.00	0.00	31.53	41.18	11.71	29.09	20.72	22.52	11.71	0.00	3.60
reni	17.31	3.85	0.00	24.04	33.98	36.54	11.65	4.85	8.74	3.88	0.97	0.00
rock1	24.00	25.00	4.00	12.00	25.25	4.00	23.00	7.00	19.00	1.00	1.00	2.00
rxra	54.20	24.43	2.29	30.53	39.32	27.48	7.69	29.77	35.88	0.76	0.00	35.11
sahh	12.70	0.00	0.00	42.86	43.33	55.56	30.16	22.22	0.00	0.00	0.00	0.00
src	59.16	50.38	1.91	14.31	12.21	7.82	14.76	5.53	11.83	1.53	1.72	13.17
tgfr1	54.89	31.58	10.53	38.35	44.36	18.05	25.56	10.53	28.57	0.75	0.00	1.50
thb	58.25	0.00	0.00	31.07	35.79	16.50	15.53	26.21	34.95	1.94	0.00	1.94
thrb	54.66	34.27	2.17	32.75	39.47	27.55	33.11	1.52	35.14	7.38	5.86	0.00
try1	54.79	42.09	4.23	42.76	44.19	40.98	50.56	2.67	22.94	9.35	3.34	0.22
tryb1	12.84	15.54	1.35	33.78	28.57	19.59	27.89	8.11	2.03	7.43	0.68	0.00
tysy	48.62	0.00	3.67	45.87	38.53	23.85	18.35	22.94	30.28	3.67	2.75	0.00
urok	53.70	48.77	2.47	43.21	53.70	12.96	47.53	8.02	12.35	2.47	0.00	3.09
vgfr2	37.90	36.19	4.65	20.54	17.00	4.65	31.68	17.36	22.74	5.87	0.00	3.67
wee1	55.88	16.67	0.00	61.76	59.80	52.94	40.20	54.46	59.41	1.98	0.00	0.98
xiap	32.00	16.00	0.00	26.00	50.51	37.00	27.00	10.10	35.35	0.00	4.04	0.00

Table S2: DUD-E per-target EF_1 scores. Abbreviations as in Table S1.

	D-G	D-R	DDTA	Gold	Glide	Surflex	Flexx	Vina	GNINA	RF	NN	Bsl.
aa2ar	0.53	0.00	0.05	0.29	0.13	0.32	0.11	0.06	0.14	0.04	0.01	0.04
abl1	0.73	0.63	0.12	0.46	0.33	0.30	0.48	0.25	0.34	0.19	0.03	0.14
ace	0.48	0.52	0.00	0.27	0.09	0.07	0.03	0.04	0.08	0.10	0.10	0.00
aces	0.38	0.09	0.14	0.36	0.16	0.34	0.03	0.25	0.27	0.09	0.03	0.07
ada	0.85	0.67	0.03	0.32	0.15	0.18	0.20	0.02	0.23	0.10	0.00	0.00
ada17	0.95	0.89	0.01	0.34	0.43	0.57	0.04	0.42	0.48	0.07	0.07	0.06
adrb1	0.38	0.01	0.04	0.45	0.32	0.26	0.18	0.08	0.08	0.03	0.03	0.01
adrb2	0.45	0.03	0.04	0.42	0.47	0.33	0.34	0.09	0.13	0.02	0.06	0.02
akt1	0.36	0.58	0.10	0.38	0.21	0.08	0.10	0.13	0.11	0.04	0.01	0.03
akt2	0.50	0.28	0.10	0.63	0.42	0.24	0.24	0.39	0.22	0.02	0.05	0.07
aldr	0.11	0.04	0.01	0.40	0.43	0.15	0.22	0.16	0.17	0.03	0.01	0.04
ampc	0.26	0.23	0.00	0.04	0.09	0.02	0.04	0.02	0.02	0.01	0.01	0.00
andr	0.60	0.38	0.02	0.04	0.42	0.08	0.01	0.31	0.17	0.03	0.04	0.05
aofb	0.05	0.02	0.02	0.27	0.14	0.10	0.11	0.16	0.04	0.02	0.02	0.07
bace1	0.77	0.33	0.02	0.41	0.26	0.29	0.21	0.09	0.32	0.30	0.03	0.01
braf	0.71	0.67	0.09	0.39	0.50	0.10	0.41	0.27	0.34	0.20	0.03	0.05
cah2	0.92	0.89	0.05	0.29	0.08	0.06	0.13	0.01	0.44	0.30	0.06	0.24
casp3	0.63	0.00	0.01	0.49	0.46	0.23	0.38	0.05	0.30	0.04	0.07	0.01
cdk2	0.74	0.52	0.07	0.29	0.50	0.07	0.22	0.17	0.37	0.02	0.03	0.17
comt	0.86	0.08	0.00	0.82	0.95	0.05	0.15	0.06	0.02	0.00	0.06	0.00
cp2c9	0.17	0.09	0.03	0.12	0.04	0.05	0.17	0.05	0.08	0.09	0.01	0.01
cp3a4	0.05	0.06	0.05	0.22	0.17	0.14	0.07	0.04	0.03	0.07	0.01	0.06
csf1r	0.67	0.44	0.11	0.34	0.31	0.05	0.38	0.05	0.31	NaN	NaN	0.07
cxcr4	0.43	0.14	0.03	0.11	0.01	0.26	0.01	0.00	0.33	0.00	0.10	0.01
def	0.97	0.82	0.00	0.48	0.14	0.59	0.01	0.20	0.58	0.08	0.04	0.00
dhi1	0.00	0.05	0.02	0.16	0.13	0.09	0.01	0.09	0.20	0.12	0.04	0.03
dpp4	0.44	0.07	0.08	0.30	0.22	0.10	0.22	0.02	0.23	0.02	0.06	0.04
drd3	0.12	0.02	0.02	0.18	0.04	0.13	0.05	0.10	0.14	0.08	0.03	0.08
dyr	0.80	0.69	0.07	0.66	0.47	0.40	0.17	0.12	0.44	0.03	0.04	0.04
egfr	0.87	0.70	0.05	0.40	0.41	0.22	0.31	0.10	0.35	0.06	0.06	0.14
esr1	0.88	0.20	0.04	0.42	0.81	0.47	0.51	0.35	0.43	0.00	0.02	0.03
esr2	0.80	0.21	0.04	0.31	0.75	0.39	0.51	0.28	0.46	0.00	0.01	0.03
fa10	0.70	0.62	0.11	0.72	0.31	0.24	0.72	0.38	0.61	0.31	0.03	0.06
fa7	0.92	0.72	0.07	0.77	0.71	0.73	0.90	0.28	0.52	0.35	0.02	0.00
fabp4	0.77	0.33	0.00	0.50	0.48	0.10	0.33	0.43	0.01	0.05	0.00	0.00
fak1	0.98	0.93	0.03	0.52	0.33	0.09	0.31	0.33	0.43	0.05	0.00	0.14
fgfr1	0.38	0.36	0.44	0.83	0.04	0.28	0.30	1.00	0.66	1.00	1.00	0.30
fkb1a	0.55	0.26	0.00	0.39	0.71	0.19	0.01	0.13	0.09	0.03	0.01	0.03
fnta	0.67	0.05	0.02	0.32	0.12	0.13	0.11	0.05	0.13	0.11	0.03	0.03
fpps	0.01	0.02	0.00	0.97	0.01	0.03	0.07	0.00	0.52	0.00	0.92	0.00
gcr	0.16	0.27	0.04	0.13	0.25	0.26	0.13	0.24	0.29	0.05	0.06	0.07
glcm	0.01	0.07	0.03	0.40	0.18	0.49	0.16	0.00	0.10	0.00	0.05	0.00

gria2	0.23	0.23	0.03	0.23	0.48	0.14	0.13	0.17	0.30	0.07	0.14	0.05
grik1	0.63	0.48	0.03	0.47	0.33	0.18	0.38	0.08	0.20	0.03	0.06	0.03
hdac2	0.87	0.78	0.06	0.32	0.27	0.26	0.29	0.24	0.09	0.08	0.05	0.09
hdac8	0.93	0.86	0.04	0.21	0.10	0.09	0.23	0.34	0.31	0.07	0.02	0.12
hivint	0.01	0.01	0.01	0.17	0.04	0.07	0.07	0.05	0.01	0.00	0.00	0.02
hivpr	0.73	0.41	0.03	0.28	0.16	0.11	0.04	0.09	0.45	0.36	0.01	0.11
hivrt	0.31	0.05	0.01	0.23	0.41	0.09	0.05	0.09	0.22	0.02	0.05	0.10
hmdh	0.71	0.70	0.01	0.42	0.69	0.34	0.05	0.10	0.65	0.10	0.04	0.01
hs90a	0.69	0.27	0.05	0.26	0.03	0.02	0.03	0.00	0.17	0.00	0.04	0.03
hxk4	0.32	0.07	0.05	0.31	0.38	0.03	0.09	0.05	0.31	0.01	0.00	0.27
igf1r	0.78	0.69	0.06	0.46	0.50	0.19	0.47	0.25	0.48	0.20	0.04	0.05
inha	0.38	0.00	0.00	0.55	0.15	0.19	0.12	0.20	0.04	0.03	0.00	0.01
ital	0.69	0.20	0.00	0.12	0.13	0.04	0.03	0.01	0.11	0.05	0.01	0.06
jak2	0.90	0.75	0.12	0.49	0.51	0.21	0.16	0.26	0.47	0.13	0.06	0.15
kif11	0.46	0.27	0.01	0.54	0.59	0.11	0.09	0.44	0.57	0.29	0.01	0.07
kit	0.60	0.52	0.07	0.25	0.11	0.06	0.16	0.10	0.22	0.12	0.03	0.09
kith	0.00	0.01	0.00	0.30	0.63	0.70	0.08	0.51	0.61	0.06	0.04	0.00
kpcb	0.77	0.50	0.01	0.50	0.69	0.44	0.44	0.46	0.36	0.03	0.04	0.13
lck	0.74	0.67	0.07	0.26	0.39	0.22	0.31	0.16	0.26	0.07	0.02	0.06
lkha4	0.85	0.57	0.00	0.28	0.57	0.34	0.15	0.29	0.30	0.02	0.00	0.04
mapk2	0.70	0.51	0.26	0.43	0.49	0.05	0.20	0.27	0.31	0.04	0.03	0.12
mcr	0.51	0.38	0.02	0.05	0.39	0.06	0.01	0.14	0.23	0.11	0.20	0.11
met	0.84	0.80	0.03	0.61	0.44	0.15	0.35	0.22	0.56	0.32	0.03	0.05
mk01	0.87	0.74	0.05	0.44	0.28	0.04	0.38	0.11	0.19	0.11	0.06	0.02
mk10	0.68	0.46	0.10	0.41	0.26	0.07	0.25	0.14	0.13	0.07	0.03	0.09
mk14	0.87	0.45	0.06	0.26	0.36	0.06	0.26	0.13	0.32	0.13	0.02	0.12
mmp13	0.95	0.88	0.03	0.40	0.30	0.24	0.08	0.08	0.17	0.10	0.04	0.17
mp2k1	0.41	0.44	0.01	0.37	0.22	0.02	0.16	0.01	0.13	0.02	0.07	0.14
nos1	0.05	0.02	0.04	0.30	0.20	0.33	0.14	0.03	0.13	0.01	0.04	0.02
nram	0.80	0.67	0.00	0.39	0.68	0.40	0.21	0.00	0.30	0.01	0.03	0.00
pa2ga	0.66	0.43	0.04	0.34	0.59	0.06	0.32	0.02	0.16	0.03	0.02	0.01
parp1	0.58	0.33	0.03	0.24	0.67	0.32	0.22	0.26	0.31	0.06	0.02	0.03
pde5a	0.42	0.22	0.06	0.18	0.34	0.15	0.04	0.19	0.24	0.02	0.02	0.03
pgh1	0.00	0.00	0.07	0.25	0.30	0.16	0.09	0.11	0.17	0.04	0.01	0.19
pgh2	0.02	0.01	0.11	0.33	0.60	0.28	0.22	0.45	0.29	0.04	0.02	0.24
plk1	0.51	0.60	0.00	0.49	0.62	0.07	0.19	0.03	0.61	0.11	0.09	0.03
pnph	0.97	0.88	0.30	0.47	0.16	0.18	0.17	0.20	0.57	0.01	0.04	0.06
ppara	0.84	0.41	0.04	0.34	0.21	0.26	0.10	0.14	0.11	0.02	0.04	0.02
ppard	0.86	0.62	0.07	0.24	0.11	0.24	0.04	0.05	0.08	0.04	0.01	0.04
pparg	0.78	0.18	0.03	0.34	0.17	0.11	0.04	0.13	0.12	0.08	0.03	0.03
prgr	0.40	0.19	0.07	0.07	0.22	0.08	0.09	0.22	0.32	0.05	0.09	0.16
ptn1	0.42	0.28	0.03	0.66	0.34	0.23	0.28	0.45	0.45	0.20	0.08	0.04
pur2	1.00	0.29	0.16	0.95	0.97	0.98	0.98	0.15	0.92	0.00	0.29	0.01
pygm	0.00	0.02	0.03	0.19	0.02	0.01	0.13	0.04	0.08	0.00	0.20	0.00
pyrd	0.02	0.02	0.00	0.52	0.62	0.25	0.49	0.34	0.34	0.18	0.00	0.07
reni	0.26	0.07	0.01	0.44	0.48	0.56	0.21	0.11	0.15	0.06	0.02	0.00
rock1	0.35	0.40	0.06	0.24	0.41	0.06	0.39	0.10	0.29	0.02	0.02	0.04
rxra	0.83	0.44	0.05	0.52	0.84	0.53	0.24	0.51	0.58	0.02	0.01	0.59
sahh	0.23	0.01	0.00	0.69	0.96	0.87	0.58	0.41	0.04	0.00	0.08	0.00
src	0.82	0.76	0.06	0.24	0.23	0.14	0.24	0.09	0.27	0.04	0.04	0.21
tgfr1	0.82	0.50	0.14	0.60	0.67	0.29	0.43	0.23	0.47	0.02	0.00	0.03
thb	0.76	0.00	0.02	0.46	0.61	0.31	0.28	0.43	0.54	0.03	0.02	0.04
thrb	0.88	0.59	0.06	0.53	0.65	0.48	0.55	0.07	0.57	0.13	0.12	0.01
try1	0.89	0.70	0.09	0.67	0.69	0.68	0.78	0.07	0.43	0.18	0.08	0.01
tryb1	0.28	0.29	0.03	0.60	0.47	0.38	0.45	0.16	0.07	0.16	0.03	0.01
tysy	0.73	0.00	0.07	0.70	0.64	0.42	0.32	0.36	0.49	0.08	0.05	0.03
urok	0.80	0.73	0.06	0.66	0.79	0.23	0.70	0.15	0.25	0.05	0.02	0.08
vgfr2	0.59	0.60	0.08	0.35	0.30	0.08	0.50	0.28	0.38	0.12	0.01	0.08
wee1	0.93	0.25	0.00	0.89	0.99	0.78	0.65	0.81	0.84	0.08	0.01	0.02
xiap	0.56	0.29	0.00	0.50	0.77	0.64	0.58	0.16	0.59	0.01	0.09	0.00

Table S3: DUD-E per-target $\text{BEDROC}_{80.5}$ scores. Abbreviations as in Table S1.